Andean Geology 47 (3): 469-507. September, 2020
doi: 10.5027/andgeoV47n3-3035

Andean Geology
www.andeangeology.cl

Tectonic setting of Cretaceous porphyry copper deposits of northern Chile (28°-30° S) and its relations with magmatic evolution and metallogeny

***Christian Creixell[1], Javier Fuentes[2], Hessel Bierma[2], Esteban Salazar[1]**

[1] *Servicio Nacional de Geología y Minería, Av. Santa María 0104, Providencia, Santiago, Chile. christian.creixell@sernageomin.cl; esteban.salazar@sernageomin.cl*

[2] *Private Consultans. Augusto Leguía Norte 115, Santiago, Chile. javier.fuentess@yahoo.com; hessel.bierma@gmail.com*

** Corresponding author: christian.creixell@sernageomin.cl*

ABSTRACT. Cretaceous porphyry copper deposits of northern Chile (28º-29º30' S) are genetically related with dacitic to dioritic porphyries and they represent a still poorly-explored target for Cu resources. The porphyries correspond to stocks distributed into two separated discontinuous NS trending belts of different age. The location of these porphyries is generally adjacent to orogen-parallel major fault systems that extend along the studied segment and also have a marked temporal relationship with deformation events registered along these structures. A first episode of Cu-bearing porphyry emplacement took place between 116 and 104 Ma (Mina Unión or Frontera, Cachiyuyo, Punta Colorada, Dos Amigos, Tricolor porphyries). These Early Cretaceous dacite to diorite porphyries are spatially associated with the eastern segments of the Atacama Fault System, which records sinistral transpression that started at 121 Ma producing ground uplift, consequent denudation and exhumation of the Early Cretaceous magmatic arc. This resulted in a change from marine to continental deposition with an angular unconformity in the site of the back-arc basin after of eastward migration of the deformation around 112-110 Ma. At the scale of the continental margin, this deformation is correlated with early stage of the Mochica Orogenic event described in Perú. A second episode of Cu-bearing porphyry emplacement occurred between 92 and 87 Ma (Elisa, Johana, Las Campanas and La Verde deposits), which are spatially and temporally associated with the regional-scale Las Cañas-El Torito reverse fault, active between 89 and 84 Ma, during the Peruvian Orogenic Phase. This fault up thrust to the west part of the Chañarcillo Group rocks (Lower Cretaceous) over the younger upper levels of the Cerrillos Formation (Upper Cretaceous). The integrated geological mapping and geochemical data of the Early to Late Cretaceous volcanic rocks indicates that both Early Cretaceous sinistral transpression and Late Cretaceous east-west compression were not significant in promote changes in magma genesis, except for slight changes in trace element ratios (increase in Th/Ta, Nb/Ta and La/Yb) suggesting that the Late Cretaceous deformation event produced only slightly increase in crustal thickness (>40 km), but far from being comparable to major Cenozoic orogenic phases, at least along the magmatic arc to back-arc domains in the study area. Finally, our study give insights about regional geological parameters that can be used as a first order guide for exploration of Cu resources along Cretaceous magmatic belts of northern Chile, where both Early and Late Cretaceous Cu-bearing porphyry intrusions are restricted to a large structural block bounded to the west and east by Cretaceous fault systems.

Keywords: Cretaceous, Central Andes, Porphyry copper, Metallogenesis, Orogenesis.

RESUMEN. Marco tectónico de los depósitos de pórfidos cupríferos cretácicos del norte de Chile (28º-30º S) y sus vínculos con la evolución magmática y la metalogénesis. Los pórfidos cupríferos de edad cretácica del norte de Chile (28°-29°30' S) están genéticamente asociados a pórfidos de composición dacítica a dioríticay representan un objetivo pobremente explorados por recursos de cobre. Estos pórfidos corresponden a stocks distribuidos en dos franjas de orientación NS discontinuas de diferente edad. Ellos se ubican generalmente adyacente a sistemas de fallas mayores, paralelas al orógeno andino, que se extienden a lo largo del segmento estudiado y tienen una marcada relación temporal con eventos de deformación tectónica registrados a lo largo de estas estructuras. Un primer episodio de emplazamiento de pórfidos tuvo lugar entre 116 y 104 Ma (pórfidos Mina Unión o Frontera, Cachiyuyo, Punta Colorada, Dos Amigos, Tricolor). Estos pórfidos dacíticos a dioríticos del Cretácico Inferior están espacialmente asociados con los segmentos

orientales del Sistema de Falla de Atacama, el cual registra transpresión sinistral que comenzó a los 121 Ma, y produjo el alzamiento y la consecuente denudación y exhumación del arco magmático del Cretácico Inferior. Tras la migración hacia el este de la deformación, alrededor de los 112-110 Ma, se originó un cambio en el régimen de sedimentación, desde marino a continental, marcado por una discordancia angular, en la cuenca de trasarco. A la escala del margen continental, esta deformación se correlaciona con la etapa temprana del evento orogénico Mochica descrito en Perú. Un segundo episodio de emplazamiento de pórfidos ocurrió entre 92 y 87 Ma (pórfidos Elisa, Johana, Las Campanas y La Verde), los cuales están espacial y temporalmente asociados con la falla inversa Las Cañas-El Torito, de escala regional, que estuvo activa entre 89 y 84 Ma, durante la Fase Orogénica Peruana. Esta falla desplaza hacia el oeste parte de las rocas del Grupo Chañarcillo (Cretácico Inferior) y los dispone sobre los niveles más jóvenes y superiores de la Formación Cerrillos (Cretácico Superior). La integración del mapeo geológico y los datos geoquímicos de las rocas volcánicas del Cretácico Temprano a Tardío indica que ambos eventos tectónicos que las afectaron, la transpresión sinistral del Cretácico Inferior y la compresión este-oeste del Cretácico Superior no fueron significativas en promover cambios en la génesis de los magmas, excepto por ligeros cambios en razones de elementos en trazas (incrementos en Th/Ta, Nb/Ta y La/Yb), que sugieren que el evento de deformación del Cretácico Superior produjo aumentos ligeros de espesor cortical (>40 km), pero aun así lejos de ser comparables a los cambios de espesor cortical originados por las mayores fases orogénicas cenozoicas, al menos en los dominios del arco magmático y del trasarco en el área de estudio. Finalmente, nuestro estudio da una idea de parámetros geológicos regionales que pueden ser usados como una guía de primer orden para la exploración de pórfidos de cobre a lo largo de las franjas magmáticas cretácicas del norte de Chile, donde intrusiones portadoras de Cu del Cretácico Inferior y Superior están restringidas a un gran bloque estructural limitado por el oeste y por el este por sistemas de fallas cretácicos.

Palabras clave: Cretácico, Andes centrales, Pórfido de cobre, Metalogénesis, Orogénesis.

1. Introduction

The distribution of metallic ore deposits along the southern central Andes has been typically characterized as various margin-parallel NS trending metallogenic belts of specific ages and broad geological setting (*e.g.*, Sillitoe, 1981, 1991, 2003; Camus, 2003; Sillitoe and Perelló, 2005). The Jurassic-Cretaceous belt of the Coastal Cordillera in Chile is characterized mostly by Cu strata-bound, stratabound and vein-type Iron oxide-copper-gold (IOCG) and iron oxide-apatite (IOA) deposits, all of these associated with the Jurassic and Cretaceous arc magmatism and characteristically associated with extensional tectonics in an active continental margin (*e.g.*, Vivallo y Henríquez, 1998; Sillitoe, 2003). Farther east, along the Domeyko Cordillera, in northern Chile, porphyry copper deposits of Eocene-Oligocene age are distributed in a longitudinal belt, spatially associated with the Eocene-Oligocene arc and the transpressive/compressive Domeyko Fault System (Boric *et al*., 1990), which points to a major structural control on the magmatism and mineralization for this time span (*e.g.*, Mpodozis and Cornejo, 2012). A younger belt of world-class porphyry-Cu-Mo deposits of Late Miocene age is located east of the Eocene-Oligocene arc, along the high Andes of central Chile, including the Los Pelambres, Río Blanco-Los Bronces, Los Sulfatos and El Teniente porphyry copper deposits. These ore deposits are spatially associated to the Neogene magmatic arc, developed in a thickened crust.

Porphyry copper deposits are outstanding metallogenic features of active continental margins and several world-class metal deposits are present in this environment. These deposits are mostly present in active continental margins and cordilleran margins (Sillitoe, 1998; Kloppenburg *et al.*, 2010; Mpodozis and Cornejo, 2012), but minor occurrences also have been recognized in extensional settings, such those described in Turkey and southeastern China (Sánchez *et al*., 2016; Piquer *et al*., 2017) and collisional settings (*i.e.*, Zhang and Hou, 2018; Richards, 2009). Several hypothesis has been proposed to explain the genesis of large (giant) porphyry copper deposits, and for the case of the Chilean Andes, these can be limited for the Cenozoic examples, where specific compositional and tectonic features such as thickened crust, compressional/transpressive setting, high water content in magmas or high oxidation state for it, has been postulated (Oyarzún *et al*., 2001; Bissig *et al*., 2003; Reich *et al*., 2003, among others). The case is different for a still not well known belt of Cretaceous Cu-porphyries recognized at north Chile (*e.g.*, Reyes, 1991; Maksaev *et al*., 2007, 2010; Sillitoe and Perelló, 2005; Richards *et al*., 2017) which are largely smaller and lower in grade relative to Cenozoic deposits, and are spatially and temporally associated to

Cretaceous arc magmatism, which overall developed under extensional conditions. In the same way, this arc magmatism and the Cretaceous Cu-porphyries are also spatially associated with a well-known Cretaceous metallogenic belt characterized mostly by IOCG and IOA deposits (*i.e.*, Sillitoe, 2003; Maksaev *et al*., 2007).

In recent years, exploration activities have turned to a renewed attention to this cretaceous porphyry copper belt of northern Chile, distributed mostly between 26º and 31º S. This belt is characterized by the presence of small (<5 km^2) porphyry intrusions and subvolcanic rocks of dacite/granodiorite to diorite composition of Lower to Upper Cretaceous age. Most known examples in this kind of ore deposits correspond to the Inca de Oro and Dos Amigos districts (Matthews *et al.*, 2006; Maksaev *et al.*, 2007, 2010), but the largest producer from this belt is the Andacollo Cu-Au porphyry, located at ~30°30' S (Llaumett, 1975; Reyes, 1991; Richards *et al.*, 2017).

In this work, we present new constrains on the age of some of these Early and Late Cretaceous Cu-Au porphyries located between 28º and 30º S, throughout seven new zircon U-Pb ages, which were obtained in the Geochronology Laboratory of University of Tasmania and the Isotope Geology Laboratory of SERNAGEOMIN, with the aim of refining the crystallization age of these ore-bearing dacite porphyries. Moreover, we present new geological constraints with the objective to refine our knowledge on the tectonic regime associated with the emplacement of these deposits, based on a preliminar work presented by Creixell *et al.* (2015) and a more advanced analysis of the Cretaceous regional geology and stratigraphy, through field observations of regional-scale structures and key stratigraphic relationship among Cretaceous geological units, including the Chañarcillo Group and the Punta del Cobre, Cerrillos and Viñita formations. Also, the compositional evolution of the Cretaceous magmatism has been investigated throughout a set of 71 samples of Cretaceous volcanic rocks and dacite porhyries, analyzed for major, trace and rare earth elements. Most of these observations have been focused to investigate the spatial and temporal relationship between the emplacement of the Cretaceous intrusions related to porphyry copper mineralization and discrete events of transpressive and compressive deformation between 28º and 30º S. The final aim of this paper is to establish genetic temporal and spatial relationship between these relatively small porphyry copper deposits and tectonic deformation events that occurred during the Cretaceous.

Analytical procedures for U-Pb geochronology and geochemistry are included, together with analytical data, as Appendixes (Table 1A for U-Pb geochronology and Table 2A for geochemical analyses).

2. Regional tectonic setting

The early evolution of the magmatic arc of the southern central Andes, from Triassic to Early Cretaceous time span, was associated with crustal extension along the continental margin (Mpodozis and Ramos, 1989; Grocott and Taylor, 2002; Haschke *et al.*, 2002). The magmatic source during this stage was dominated by additions of primitive melts from the asthenospheric mantle to the crust (*e.g.*, Lucassen *et al.*, 2006). The paleogeographic configuration of the active continental margin consisted of a submarine to subaerial magmatic arc, characterized by effusion of large volume of intermediate to mafic lavas (*e.g.*, La Negra Formation, García, 1967; Oliveros *et al.*, 2007; Punta del Cobre Formation; Segerstrom and Ruiz, 1962) and emplacement of composite batholiths. An eastward parallel back-arc basin was dominated by marine sedimentation during the Jurassic to Early Cretaceous (Tarapacá basin), but with restricted episodes of subaerial deposition (Oliveros *et al.*, 2012). This geodynamic setting remained in steady state during the Jurassic and Early Cretaceous, except for some discrete episodes of intra-arc transpression along major fault systems for the Late Jurassic (Scheuber *et al.*, 1994; Creixell *et al.*, 2011; Ring *et al.*, 2012) and Early Cretaceous (Scheuber and González, 1999; Arévalo and Creixell, 2009). Since about 100-85 Ma, several compressive to transpressive events were registered along the southern Central Andes margin, marking a change from marine to subaerial deposition along the backarc, inception of a foreland basin instead of a back-arc, progressive eastward shift of the axis of the magmatic arc and dominance of more felsic compositions of igneous rocks (*e.g.*, Richards *et al*., 2017). These Late Cretaceous deformation episodes have been proposed as the first pulses of Andean orogenesis in the central Andes by several authors (*e.g.*, Coutand *et al.*, 2001; Cobbold and Rosello, 2003; Arriagada *et al.*, 2006; Bascuñan *et al.*, 2015). These events led to recognition of regional-scale

unconformity surfaces or displacements along major fault systems (*e.g.*, Sánchez and Emparán, 2006). Moreover, discrete changes in trace element ratios (*e.g.*, La/Yb) of arc magmas have been described associated with Cretaceous deformation events and also for Cenozoic ones, in the last case associated with crustal thickening (Kay and Mpodozis, 2001; Haschke *et al.*, 2002; Mpodozis and Cornejo, 2012).

2.1. Current knowledge on Cretaceous tectonics of the southern central Andes

During the Early Cretaceous, some authors have identified the occurrence of one or more tectonic events that disturbed the dominant extensional/transtensional tectonic setting along the arc and backarc. Along the western part of the study area, Arévalo and Creixell (2009), based on kinematic analysis of brittle and ductile faults, including S-C mylonites and porphyroclasts, and radiometric dating of mylonites, inferred that a sinistral transpressive regime of deformation along the Atacama Fault System (AFZ) took place as early as 121 Ma and extended until at least 117 Ma, controlling the emplacement of plutonic complexes and IOCG deposits and following a stage of along-arc extension, suggested by geometry of fault-bounded plutons. For the same AFZ system farther north (22º-26º S), Scheuber and González (1999) proposed that a sinistral transpression stage started roughly at 125 Ma, based on changes in the orientation of dike swarms, and after a stage of arc-normal extension. Dallmeyer *et al.* (1996), on the basis of $^{40}Ar/^{39}Ar$ dating on mylonites, inferred a similar age ~126 Ma for the change from vertical to left-lateral displacements along the AFZ. Arancibia (2004), based on kinematic analysis and $^{40}Ar/^{39}Ar$ dating of neoformed minerals, showed that the Silla del Gobernador Shear Zone, a regional-scale fault with ductile deformation located along the Coastal Cordillera at about 32º S, displayed west-directed reverse shearing between 109 and 97.8 Ma.

At regional scale, several sources of data indicate indirectly that the plutonic rocks of the Coastal Cordillera were exhumed during the Cretaceous, pointing to possible deformation events during this period. Gana and Zentilli (2000) inferred that Carboniferous granitoids exposed along the Coastal Cordillera at 33º S were exhumed at about 106-98 Ma, based on apatite fission track ages. Sedimentary record of Cretaceous stratified rock sequences of central Chile also suggests that exhumation and subsequent erosion of uplifted blocks took place during the Cretaceous. Recently, Boyce *et al.* (2020), based on the stratigraphic record of terrigenous strata of the Early Cretaceous Las Chilcas Formation in central Chile (33º S), proposed that this unit represents the sedimentary filling of a proximal foreland basin, associated with compressive pulses, basin inversion and orogenic processes that took place between 105 and 83 Ma. In addition, Merino *et al.* (2013) interpreted that stratigraphy and detrital zircon ages of Late Cretaceous continental sedimentary deposits exposed in the Frontal Cordillera of Chile between 28º30' and 29º30' S (ascribed to the Pucalume Formation) registered the deposition of synorogenic sedimentary rocks associated with a regional tectonic deformation event ("Peruvian phase") with basement exhumation at about 90 Ma. In the same way, Bascuñan *et al.* (2015) based on stratigraphy and detrital zircon ages of Late Cretaceous sedimentary rocks in the Antofagasta region of northern Chile, suggested that at least two orogenic pulses occurred at 107 and ~80 Ma. South of 36º S, the Upper Cretaceous Neuquén Group in Argentina has been also interpreted as synorogenic deposits associated with compression and uplift of the Early Cretaceous arc located to the west, in the Chilean territory (Tunik *et al.*, 2010; Mescua *et al.*, 2013, and references therein). At regional scale, the Cretaceous deformation events indicated by the geological record of north-central Chile can be associated with two major tectonic events described for the arc and back-arc basins associated with the active continental margin: A first event, mostly known as Mochica Orogenic Phase, with an early stage around 110-105 Ma and a widespread second pulse between 100 and 95 Ma (*e.g.*, Jaillard, 1994; Jaillard and Soler, 1996; Tunik *et al.*, 2010; Menegazzo *et al.*, 2016). The second event is the Peruvian Orogenic Phase, which started around 90 Ma, and probably extended during most Late Cretaceous time (Jaillard, 1992; Haschke *et al.*, 2002; Menegazzo *et al.*, 2016).

3. Main stratigraphic and structural features in the studied segment

The geology around the study area (Fig. 1), located south of Vallenar city, comprises mostly Early to Late Cretaceous volcanic, sedimentary and plutonic rock units. These volcanic and sedimentary rocks, between

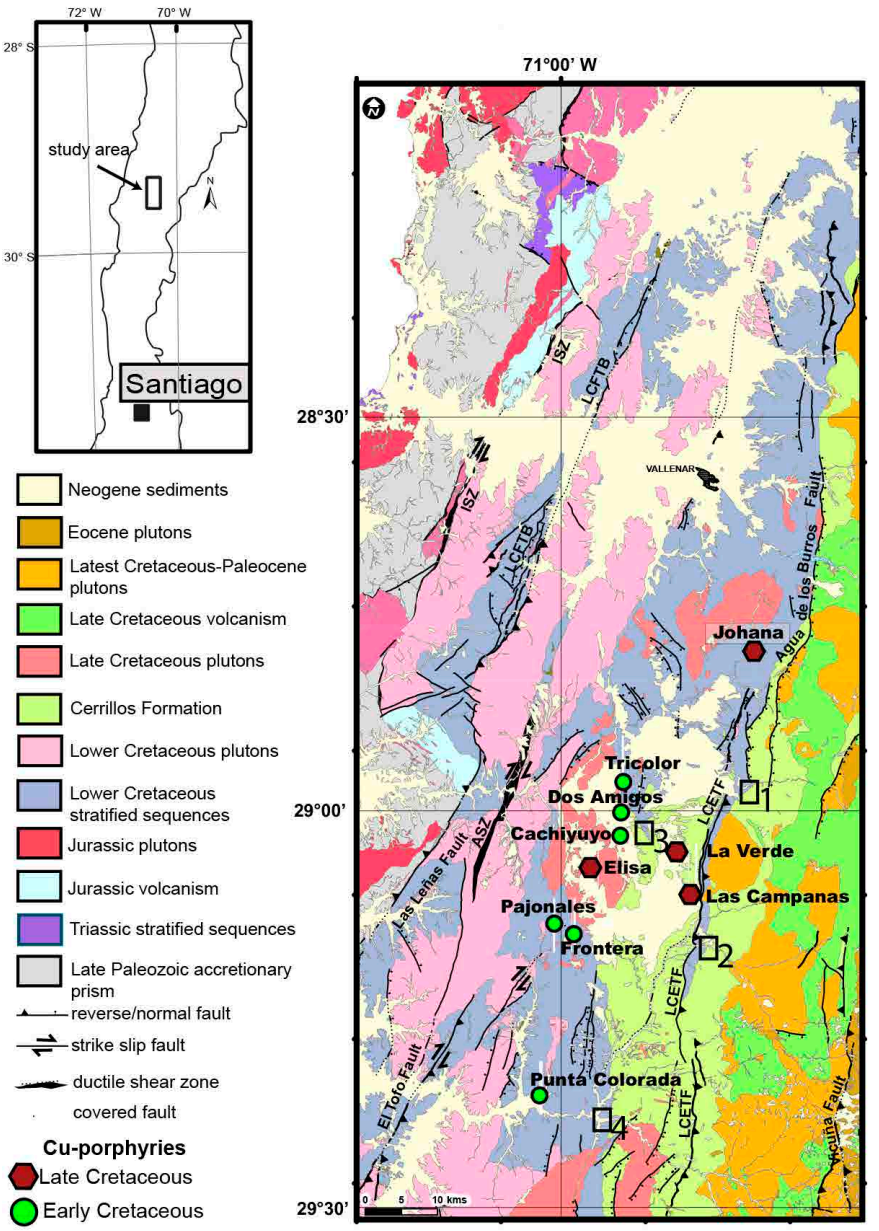

FIG. 1. Simplified geological map of coastal region of north Chile between 28° and 29°30' S, with emphasis on the Cretaceous stratified and plutonic rocks units and major structures, modified from Arévalo and Welkner (2008); Welkner *et al*. (2006), Arévalo *et al*. (2009) and Creixell *et al*. (2012, 2013). The location of studied cretaceous porphyry copper deposits is marked by green circles (Early Cretaceous) and red hexagons (Late Cretaceous). Some of the main fault systems have abbreviated names, as follows: **ISZ:** Infiernillo Shear Zone; **LCFTB:** Los Colorados Fold and Thrust Belt: **ASZ:** Algarrobo Shear Zone; **LCETF:** Las Cañas-El Torito Fault. Numbered black squares indicate the location of key stratigraphic localities mentioned in the text: **1:** Algarrobal creek; **2:** La Silla; **3:** La Verde Creek; **4:** Tres Cruces.

28° and 30° S, are distributed at regional scale, as N-S oriented belts dipping east (Fig. 1), interrupted by N-S to NNE-SSW extensional and compressional faults and fold systems. Plutonic rocks are organized along complexes of dominant dioritic composition, with progressively younger ages eastward.

3.1. Cretaceous stratigraphy

The Cretaceous stratigraphy of the area is synthetized in figure 2 and it is characterized by a lower unit corresponding to the Late Jurassic-Early Cretaceous rocks of the Punta del Cobre Formation (Segerstrom and Ruiz, 1962), mostly constituted by pyroxene-bearing andesites. In the stratigraphically lower and upper sections of the formation, these lavas are interbedded with sedimentary breccias, marine sandstones and limestones, indicating that volcanism took place under submarine conditions in several levels of the unit. An important change in facies is noted at the upper section of the Punta del Cobre Formation, where minor lavas are associated with red beds (sandstones, pyroclastic breccias, and conglomerates), with some well-recognized subaerial facies associated with explosive volcanism, dated at 118-112 Ma by Creixell *et al.* (2013). This unit, together with intermediate to mafic plutonic rocks, is ranging in age between 143 and 110 Ma (Creixell *et al.*, 2012), form the core of the Coastal Cordillera at this latitude and all these units represents the Late Jurassic to Early Cretaceous magmatic arc. A relevant feature of this arc association is that numerous IOA and IOCG deposits are present along the pluton-lava interface or along faults of the AFS (Vivallo *et al.*, 2008; Arévalo and Creixell, 2009; Arévalo *et al.*, 2009; Arredondo *et al.*, 2018). Limited age data of the mineralization and hydrothermal alteration of these deposits indicate Early Cretaceous ages that are coetaneous with arc magmatism (Vivallo *et al.*, 2008; Creixell *et al.*, 2012; Veloso *et al.*, 2016). The origin of these IOA deposits was interpreted as magmatic hydrothermal (Ruiz, 1967; Ruiz *et al.*, 1968; Bookstrom, 1977; Menard, 1995), whereas other authors favored an iron oxide ore magmas as source for these deposits (Nyström y Henríquez, 1994; Travisany *et al.*, 1995). In addition, a recent magmatic-hydrothermal model has also been proposed for the IOA deposits (Knipping *et al.*, 2015; Reich *et al.*, 2016).

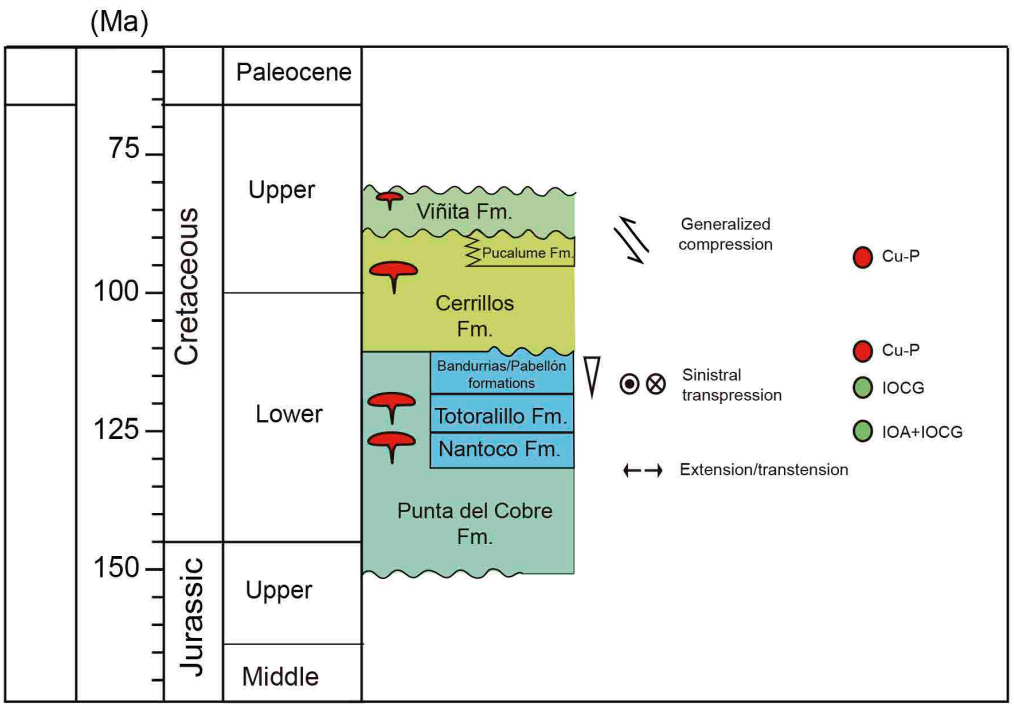

FIG. 2. Schematic and generalized stratigraphy of the study area (left column), with red ballons indicating the temporal location of main plutonic events. The tectonic setting and different styles and events of mineralization are located in the right columns. Based on Arévalo *et al.* (2009); Creixell *et al.* (2012, 2013); Salazar *et al.* (2013) and references in the text. **Cu-P:** porphyry copper deposits; **IOCG:** iron oxide copper gold deposits; **IOA:** iron oxide apatite deposits. Geological Time Scale according to Gradstein *et al.* (2012).

Early Cretaceous rock sequences exposed to the east (inland) of the magmatic arc are considered by several authors as representing a back-arc environment (*e.g.*, Mpodozis and Ramos, 1989). The Chañarcillo Group (Upper Hauterivian-Aptian, Segerstrom and Parker, 1959) is constituted by sedimentary rocks grouped in the Nantoco, Totoralillo and Pabellón formations, all these with lithologies dominated by marine limestones, with minor amounts of shales, calcareous sandstones and volcanic rocks. This unit is contemporaneous with the upper portion of the Punta del Cobre Formation, exposed *ca*. 20 km west. The Bandurrias Formation comprises brownish-red sandstones and breccias with local intercalations of andesites and Aptian-Albian fossiliferous limestones. Outcrops of the Pabellón Formation along the Pelícano and Algarrobal creeks show that upper levels of this unit are characterized by progressive variation from calcareous strata to terrigenous deposits (sandstones and conglomerates) with dominant volcanic detritus. The Early Cretaceous sequences mentioned above are covered by rocks of the Cerrillos Formation. The contact between these units is variably unconformable or conformable along the studied segment (Arévalo *et al.*, 2009; Creixell *et al.*, 2013) and is described and analyzed in more detail below (chapter 3.2.). In general terms, the Cerrillos Formation, consists of an association of subaerial terrigenous deposits and a dominant volume of volcanic rocks (lavas and tuffs) with about 1,000 meters of thickness. The age of the unit, considering several localities between Copiapó and Vallenar, was previously assigned between the Albian and the Maastrichtian (Arévalo *et al.*, 2009; Maksaev *et al.*, 2009), but for the studied segment, has been restricted between the Albian and the Coniacian by Creixell *et al.* (2013), on the basis of the recognition of a regional scale unconformity at the top of the sequence and several zircon U-Pb ages. The base of the unit has been dated by several zircon U-Pb ages 112 and 110 Ma (Maksaev *et al.*, 2009; Creixell *et al.*, 2013). The Cerrillos Formation has been separated in a lower dominantly siliciclastic member (Checo de Cobre member), and an upper volcanic member. However, the lower sedimentary member interfingers laterally, northward and southward, with volcanic facies. At Pelicano creek (La Silla locality at figure 1), the Checo de Cobre member is composed mostly of well-stratified volcanic rocks, medium to coarse grained sandstones with intercalation of green limestones, tuffs and volcanic breccias, conglomerates, and minor mudstones, (Salazar *et al*., 2015). At Los Choros creek (Tres Cruces Locality at Figure 1), the Cerrillos Formation, consists of conglomerates and tuffs (Fig. 3A), and is exposed conformable over brown-red sandstones and andesites of the Bandurrias Formation. In this locality the upper volcanic member of the Cerrillos Formation is composed mostly of andesite lavas with intercalations of rhyolite tuffs and volcanic breccias. Andesites are pyroxene bearing, but locally contain also oxidized olivine phenocrysts.

The Cerrillos Formation varies locally to the east to a sedimentary sequence of about 1,085 m thickness consisting of sedimentary breccias, lithic sandstones and conglomerates and minor intercalations of calcareous limolites of Late Cretaceous age (Turonian-Coniacian) ascribed by Creixell *et al.* (2013) to the Pucalume Formation. Both the Cerrillos and the Pucalume formations are covered unconformably by an eastward gently-dipping plateau of andesites and dacitic and rhyolitic tuffs with U-Pb ages between 84 and 78 Ma assigned to the Viñita Formation (Creixell *et al.*, 2013; Salazar *et al.*, 2013).

3.2. Unconformities

Two main unconformities are recognized along the study area. The older one is registered at the base of the Cerrillos Formation, and changes its character from north to south and west to east. In the western half of the study area, at Tres Cruces locality (Fig. 1 and 3A) this unconformity is almost absent between the Bandurrias Formation and the overlying Cerrillos Formation. The same situation is observed along the La Verde Creek locality (Fig. 1), between Pabellón and Cerrillos formations. In the eastern part of the study area, the basal contact of the Cerrillos Formation with the underlying Pabellón Formation is variable along strike both geometrically and in the facies involved. Along the Algarrobo creek (about 15 km east of the Tricolor deposit, Fig. 1), this contact is largely unconformable, where folded limestones of the Pabellón Formation are covered by sandstones and conglomerates disposed in onlap geometry over the limestones (Fig. 3E). Deformation on the limestones slightly decreases to the south, where at La Silla locality (Fig. 1) we can observe a less angularity but an erosive contact at the base of the Cerrillos Formation over the Pabellón Formation.

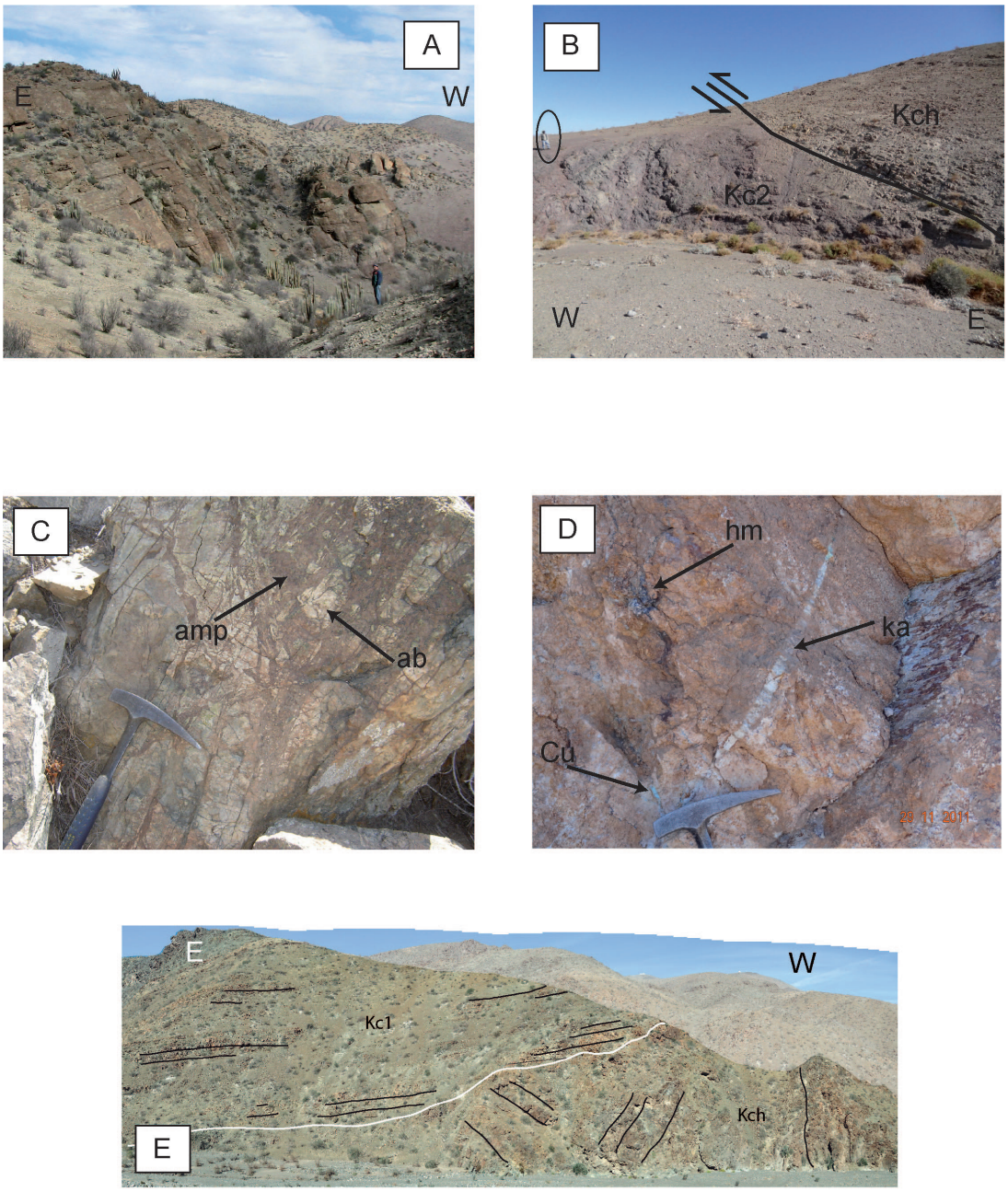

FIG. 3. Field photographs of the study area. **A.** Basal sequence of the Cerrillos Formation near Los Choros creek, consisting in gently east-dipping conglomerates, sandstones and tuffaceous sandstones, with well-developed stratification, view to the SE; **B.** Profile view of the Las Cañas fault, with limestones of the Totoralillo Formation (Kch) on the hangingwall, yuxtaposed over younger andesites of the upper member of the Cerrillos Formation (Kc2) in the footwall, view to the north. Geologist for scale at the left border of the photograph; **C.** Hydrothermal breccia located along the trace of the El Tofo fault, dated at 111 Ma by Creixell *et al.* (2012), consisting lithic clasts strongly replaced by albite and quartz (ab), in a matrix of actinolite and quartz (amp); **D.** Supergene alteration on the Early Cretaceous Cachiyuyo porphyry copper, with main replacement by silica, with late pods of hematite (hm) and kaolinite (ka) and chrysocolla veins (Cu); **E.** Unconformable stratigraphic contact between the strongly deformed Pabellón Formation (Kch) and the east-dipping Lower Member of the Cerrillos Formation (Kc1). Stratification is marked along black lines. The unconformity is marked along the white line in the figure; Algarrobo creek, view to the south. Approximate width of the photo is 70 m.

The second regional scale unconformity is observed at the contact between Cerrillos (or locally Pucalume) and the overlying Viñita Formation. The angular unconformity between these units is variable, but locally is over 40º, especially near Las Campanas observatory, where a gently inclined eastward dipping plateau of andesite lavas and acidic tuffs is disposed over largely deformed beds of the Cerrillos Formation.

In order to better constrain the age of the older unconformity and the source of detrital material involved in the upper levels of the Pabellón Formation, we obtained three U-Pb ages near the top of that sequence in two localities. One sample (MJC-81, Appendix Table 1A, Fig. 4A) of coarse-grained sandstones at La Verde Creek locality yielded a mean average zircon U-Pb age of 118.6±1.0 Ma, considering a Gaussian distribution of individual ages between 113 and 124 Ma (n=30). The nearly unimodal distribution of ages indicates that the zircon and therefore detrital sources for this sandstones are derived from volcanic materials exposed along the same section, below or directly west of the sampled levels, belonging mostly to the upper levels of the Punta del Cobre Formation. Another sample (PLC-52, Appendix Table 1A), obtained near the top of the Pabellón Formation at La Silla locality, yields a weighted mean average zircon U-Pb age of 126.1±0.1 Ma (Fig. 4B) from a single Gaussian age distribution (from a unimodal age distribution), largely older than a sample of pyroclastic breccia from the overlying sequence (Cerrillos Formation), that yields a mean average of 114.7±0.3 Ma (sample PLC-51, Appendix Table 1A, Fig. 4C), and a zircon U-Pb crystallization age of 111.5±1.2 Ma from a tuff at the same stratigraphic level (Creixell *et al*., 2013). The unimodal character of the ages for the Pabellón Formation reflects that source of detrital material comes from local volcanic sources, probably the explosive eruptions characteristics from this period of time, well preserved in the top levels of the Punta del Cobre and Bandurrias formations, and locally registered in the top levels of the Pabellón Formation, as interbedded dacite and rhyolite tuffs (Creixell *et al.*, 2013). Taking into account these data with previous paleontological and U-Pb data from Creixell *et al.* (2013) from the Pabellón and Cerrillos formations, we can restrict the age for the unconformity between both units between 116 and 110 Ma.

3.3. Faults

A western domain of structures is part of the Atacama Fault System (AFS), where preserved stratigraphic relationship and some drag folds associated to extensional displacements along older plutons, suggest that these structures were previously active as normal faults, during the Early Cretaceous, around 130 Ma (Creixell *et al*., 2012). The younger well-documented tectonic activity on these structures is lower Cretaceous in age (121-117 Ma; Arévalo and Creixell, 2009), that is younger than the age for sinistral displacements in the AFZ (*ca*. 126 Ma) further north (Dallmeyer *et al.*, 1996; Scheuber and González, 1999). Some of these faults contain ductile shear zones at pluton margins, indicating deformation coeval with pluton emplacement, whereas other faults exhibit brittle deformation and commonly occurrences of hydrothermal alteration zones. Along these structures, left-lateral transpression has been recognized, adjacent to Lower Cretaceous plutons and IOCG deposits. Main structures of this domain are grouped into the El Tofo Fault System (ETFS) where the main structures correspond to El Tofo and Las Leñas faults and La Higuera Shear Zone. To the east of the Early Cretaceous magmatic arc, normal faults spatially associated with Early Cretaceous sedimentary and volcanic sequences were documented by Arévalo *et al.* (2009) and Creixell *et al.* (2013). These faults control and affect the distribution of Lower Cretaceous back-arc sedimentary units (Bandurrias Formation and Chañarcillo Group).

Faults recognized along the eastern part of the study area exhibit mostly reverse sense of displacements (Fig. 1). The most prominent structure corresponds to the east-dipping Las Cañas-El Torito Fault (LCETF). The trace of the fault extends by about 50 km trending roughly N-S, between 28º50’ and 29º30’ S. South of 29º S, the LCETF juxtaposes calcareous marine beds of the Chañarcillo Group (Early Cretaceous) on its hanging wall over volcanic rocks of the Upper Member of the Cerrillos Formation (Creixell *et al.*, 2013), through a master fault associated with minor synthetic reverse faults over the Chañarcillo Group. Directly east of La Verde porphyry, the geometry of the master fault is exposed as a reverse fault dipping 30° east, parallel to the dip of the strata of the Totoralillo Formation over Cerrillos Formation, configuring a ramp-like geometry for the fault (Fig. 3B). The exposed footwall of the LCETF

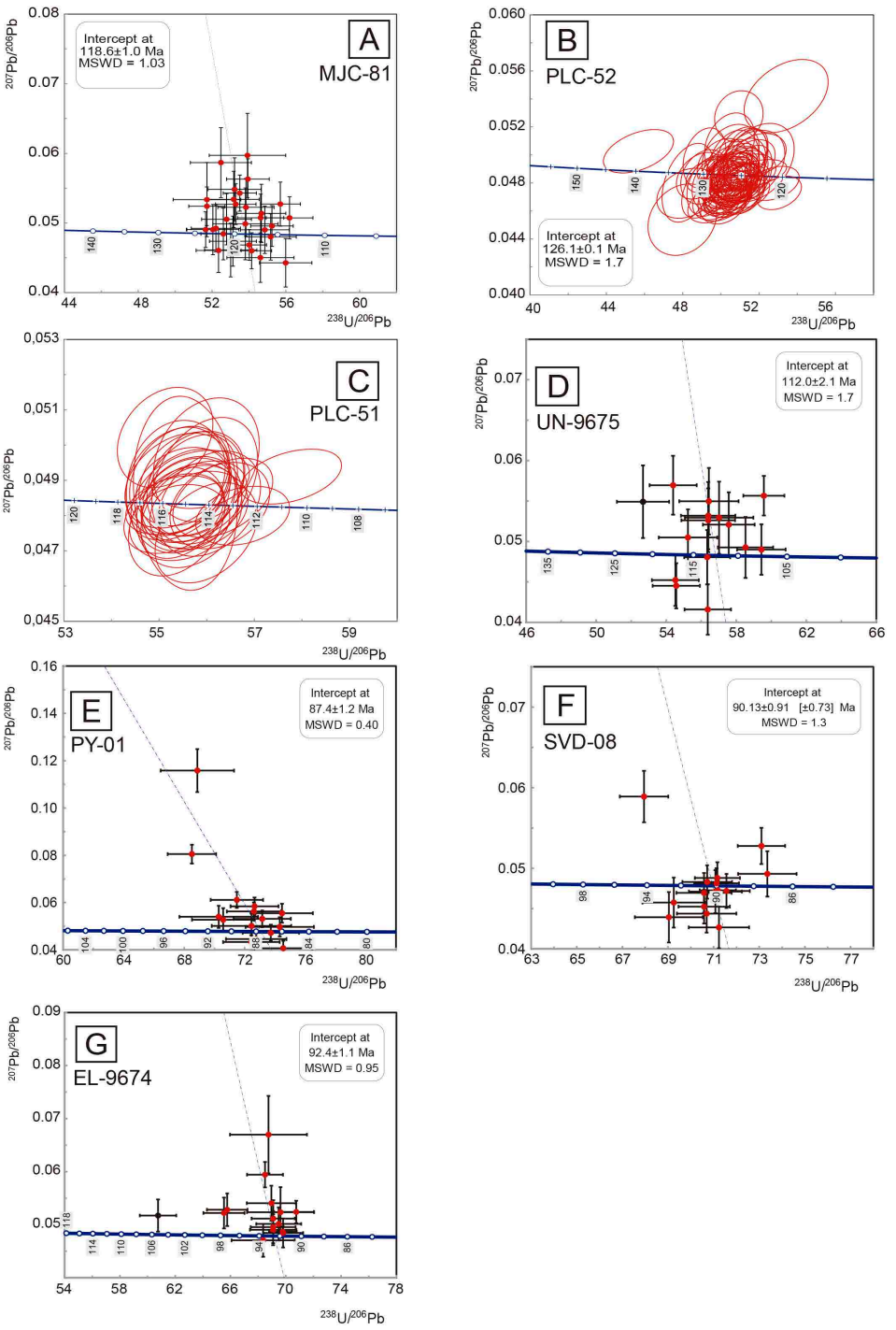

FIG. 4. Tera-Wasserburg diagrams for zircon U-Pb ages of this study; **A-B.** U-Pb ages on sedimentary rocks of the upper Pabellón Formation from the Chañarcillo Group (samples MJC-81 and PLC-52, respectively); **C.** Sample from a volcanic breccia strata of the basal part of the Cerrillos Formation (sample PLC-51); **D.** La Unión porphyry (sample UN-9675); **E.** Johana porphyry (sample PY-01); **F.** Las Campanas porphyry (sample SVD-08); **G.** Mina Elisa porphyry (sample EL-9674). Crosses and ellipses for data-point errors are at 1σ. Weighted mean age (intercept) error is at 2σ.

consists of the subhorizontal volcanic rocks of the upper member of the Cerrillos Formation truncated eastward by the fault. In the hanging wall block, the Cerrillos Formation is disposed conformably and unconformably over the Chañarcillo Group as an east-dipping succession, passively-folded over the fault ramp. Locally, folds with near vertical limbs are recognized around 29º15' S on the fault hanging wall. These contact relationship allows inferring a post-89 Ma activity for the LCETF. On the other hand, in the same hanging wall, the Cerrillos Formation is unconformably covered by the subhorizontal Viñita Formation (dated at 84 Ma, Creixell *et al.*, 2013), thus bracketing the activity of the LCETF between 89 and 84 Ma.

South of this locality, the LCETF exhibits progressively less stratigraphic displacement and near 29º30' S, deformation along the fault system is almost negligible, with no regional folding and minor stratigraphic displacement. The trace of the fault system is not recognized farther south.

4. Cretaceous dacitic and dioritic porphyry intrusives

4.1. Early Cretaceous porphyritic intrusions

Several small intrusive bodies (<5 km^2) have been recognized, hosted by volcanic rocks of the upper part of the Punta del Cobre Formation (Fig. 1). Most of these intrusives contain variable amounts and types of Cu mineralization and are spatially associated with hydrothermally altered rocks with sericitic to intermediate argillic mineral associations in several generations of events. All these intrusive bodies typically have >25% phenocrysts, fine-grained groundmass and composition ranging from diorite to granodiorite/dacite. Some of these have been recognized in porphyry copper exploration prospects at Punta Colorada, Cachiyuyo, El Pleito, Pajonales, but also in already exploited deposits, such as Mina Unión (Frontera) and Dos Amigos-Tricolor porphyry copper deposits.

At Punta Colorada prospect (Fig. 1), a dacite porphyry is intruded into andesites of the Punta del Cobre Formation. The porphyry has withish grey color, largely visible along old exploration trenches and is intruded by andesite dikes. This intrusive is also spatially related to dacite dikes intruded into the andesite of the Punta del Cobre Formation. The dacite displays a porphyritic texture and mafic inclusions with acicular amphibole (quenching texture). Phenocrysts correspond to albitized plagioclase, corroded quartz, biotite partially replaced by epidote, smectite and titanite and chloritized amphibole. The fine-grained groundmass is composed by quartz, biotite and plagioclase. Advanced argillic alteration zones are widespread in the host rock close to the dacite porphyry, with kaolinite, diaspore, silica and pyrophyllite. Chrysocolla is the main ore mineral recognized in the field, disposed widespread along rock fractures in the dacite.

At Cachiyuyo (Fig. 1), a porphyritic dacite is intruded into tuffs of the Cerrillos Formation with a remarkable reddish outcrop color. This dacite is composed by quartz, sericite altered plagioclase and chloritized amphibole phenocrysts, but the intrusive is also affected by pervasive silicification and by supergene alteration characterized by widespread limonites, kaolinite, alunite, hematite-goethite and chrysocolla veins (Fig 3D).

At Mina La Unión (Fig. 1, Frontera prospect), there is an old open pit and several small sites of past mining activity. In this prospect, a Cu-Au porphyry deposit is characterized by several porphyritic diorite intrusions hosted by andesite of the Punta del Cobre Formation, with biotite (potassic alteration) and late hematite that contains Cu (oxides and sulfides) and Au (Maksaev and Llaumett, 2015).

An important number of dacitic dikes and stocks have been recognized along the El Pleito-Melón and Los Cristales mining districts (south of the Pajonales prospect, Fig. 1), partially overprinting the Early Cretaceous IOA and IOCG deposits. In the vicinities of El Pleito mine, high temperature mineral associations associated to iron oxide deposits are partially overprinted by widespread silica+albite alteration zones spatially associated with porphyritic dacite dikes and stocks, that intrude into andesite sequences and Early Cretaceous diorite plutons. In the same area, localized advanced argillic alteration zones (andalusite+pyrophyllite+kaolinite+dickite), common for IOCG deposits are spatially associated with dacite dikes and stocks (some pyrite-bearing). Specularite-K-feldspar veins and actinolite-albite hydrothermal breccias (Fig. 3C), all these dated around 111-110 Ma (Creixell *et al.*, 2012) are apparently emplaced along Early Cretaceous faults. The dacite dikes are similar in composition to those described at Punta Colorada (Fig. 1). Morelli (2008)

reported the occurrence of dacite porphyries, dated at 116 Ma, associated to relict sericitic alteration zones, surrounded by a large argillic alteration zone at Pajonales (Fig. 1), but without evidences of porphyry-type mineralization. At the northern end of the Los Cristales district, the Totora prospect shows evidences of porphyry-type Cu-Au mineralization, associated with a quartz-diorite porphyritic intrusive with surrounding potassic alteration, but also a porphyrytic dacite intrusion. (Maksaev and Llaumett, 2015).

A slightly younger group of porphyry copper type deposits associated with porphyritic intrusives of granodiorite to tonalite composition has been described in the Dos Amigos district, close to the town of Domeyko (Fig. 1). These consist of two porphyry copper deposit centers (Tricolor and Dos Amigos), located within a large hydrothermal alteration zone of 6x1.5 km (Maksaev *et al.*, 2010). The porphyries intrude into volcanic rocks of the Punta del Cobre Formation. The granodioritic and tonalitic porphyries (At Tricolor and Dos Amigos) are characterized by presence of quartz and plagioclase phenocrysts and a fine-grained groundmass that display potassic alteration characterized by the presence of fine-grained biotite aggregates. By the other hand, the volcanic country rock, mostly andesites, display variable hydrothermal alteration, including sericitic, kaolinite-illite and propylitic mineral assemblages (Maksaev *et al*., 2010). A large hydrothermal breccia body is present close to Dos Amigos porphyry copper center, and is characterized by polymictic clasts of sericitized volcanis rocks and porphyries in a matrix of rock flour, pyrite, quartz and tourmaline, but also containing minor amounts of chalcopyrite (Maksaev *et al*., 2010). The Dos Amigos deposit, specifically its chalcocite secondary enrichment blanket was mined until 2015 (Maksaev and Llaumett, 2015).

According to zircon U-Pb dates, the age of Early Cretaceous porphyry intrusions range from 120 to 104 Ma. The oldest ones correspond to Totora diorite porphyries (120.8 and 119.5 Ma, V. Maksaev unpublished U-Pb data, in Maksaev and Llaumett, 2015) and the dacite porphyry at Pajonales (116.6±4.0 Ma, Morelli, 2008). For Punta Colorada dacite porphyry, Creixell *et al.* (2012) obtained a zircon U-Pb age of 109.7±0.9 Ma, and for the dacite porphyry at Cachiyuyo prospect, Creixell *et al.* (2013) obtained a zircon U-Pb age of 111.0±1.9 Ma. The younger (Albian) ages, between 108.5 and 104.0 Ma where obtained by Maksaev *et al.* (2010) for Dos Amigos and Tricolor porphyries, respectively. In this study, a new zircon U-Pb age of 112.0±2.1 Ma was obtained for the diorite porphyry at Mina La Unión or Frontera Prospect (Fig. 4D, sample UN-9675 in Table 1A Appendix), that is concordant with those obtained for porphyritic intrusives at Punta Colorada and Cachiyuyo prospects.

4.2. Late Cretaceous porphyritic intrusions

The porphyritic intrusives of this group are stocks of reduced exposure (<10 km^2), with associated porphyry-Cu-like deposits, mostly with past mining or present exploration activities. All of these intrusives are emplaced into andesite and dacite-andesite lavas of the Upper Member of the Cerrillos Formation. Three of these porphyry copper bearing prospects are located between 2 and 4 km to the west of the trace of the Las Cañas-El Torito Fault System (Fig. 1). The only exception corresponds to Mina Elisa, located 15 km to the west of the fault and emplaced into the Late Cretaceous Domeyko Plutonic Complex (Creixell *et al.*, 2013).

The Late Cretaceous porphyries corresponds to dacites, with variable amount of phenocrysts of embayed quartz, plagioclase and amphibole replaced by chlorite, in a fine-grained groundmass of the same minerals, often replaced by secondary quartz and sericite. Outcrops are associated with small (<3 km^2) zones with hydrothermally altered volcanic country rocks. These zones consist of sericitic alteration with hematite and late carbonate veins and variably developed supergene argillic alteration overimposed or, in the case of Las Campanas, surrounding the rocks affected by sericitic alteration.

The age of the dacitic intrusives is constrained by one zircon U-Pb age of 88.4±1.2 Ma reported by Creixell *et al.* (2013) for a dacite porphyry in the La Verde porphyry copper prospect (Fig. 1). Approximately 30 km north, in the Johana (Cortadera) porphyry copper prospect, a similar zircon U-Pb age of 87.4±1.2 Ma was obtained (Fig. 4E, sample PY-01 in Table 1 Appendix), whereas at Las Campanas (Fig. 1), a dacitic porphyry displays a zircon U-Pb age of 90.13+0.91 Ma (Fig. 4F, sample SVD-08). For a dacite porphyry intrusion at Mina Elisa (Fig. 1), we obtained a slightly older zircon U-Pb age of 92.4+1.1 Ma (Fig. 4G, sample EL-9674). The age of these intrusives is close to the age of their volcanic country rocks, in this case the upper volcanic member

of the Cerrillos Formation (92-89 Ma, Creixell *et al.*, 2013), compatible with their subvolcanic nature.

5. Geochemical trends in the Cretaceous volcanism

With the aim to study the compositional evolution through time of the Cretaceous magmatism, from 140 to 80 Ma (Punta del Cobre to Viñita formations), as a tool to trace possible changes at the source region of the magmas, we analyzed a set of 71 whole-rock samples (see Table 2A of Appendix for detailed results) for major, trace and rare earth elements (REE). Selected trace element ratios, sensitive to pressure conditions (*e.g.*, by variations in tectonic conditions or crustal thickness) were also used. The sample set include a large registry of Cretaceous volcanism including Early Cretaceous lavas from the Punta del Cobre and Bandurrias formations, and lavas and tuffs from the Cerrillos and Viñita formations, but also selected samples from porphyrytic intrusions. Details on the results and Analytical procedures are presented in the Appendix.

The general composition of Cretaceous volcanic rocks shows a large range in terms of SiO_2 contents, covering the entire range between basalt and rhyolite. For most major elements, a good correlation with SiO_2 content is observed for every sample group. It is worth to note that the Mesozoic volcanic sequences of the Central Andes are affected by low-grade regional metamorphism from low zeolite to greenschist facies (*e.g.*, Levi *et al*., 1989), so that a significant number of samples of volcanic rocks and porphyries (~35%) evidences effects of low temperature alteration, reflected by LOI>2%. In spite of this, petrographic inspection of the samples, together with relatively homogeneous behavior of strongly mobile elements, such as Ce and Rb, suggest that the effects of alteration are mostly incipient and do not affect the elements distribution for petrological analysis. Moreover, samples of porphyries affected by alteration (LOI between 3.3 and 3.5%) are indistinguishable in terms of trace element contents with respect to less altered samples of the same group. In order to minimize the possible effects of alteration or metamorphism, we focused on the composition of immobile elements, such as Th, Zr and REE. In the classification scheme based on immobile elements (Winchester and Floyd, 1977), basaltic andesites and andesites are dominant in Early Cretaceous lavas, and andesites and dacites in Late Cretaceous rocks. The youngest Cretaceous units (Viñita Formation, Fig. 5) show widespread compositions, from basalt to rhyolite. Together with progressive increase in SiO_2, the Zr/TiO_2 ratio also shows higher values towards younger units. Most samples from porphyrytic intrusions fall into the field of rhyolite/dacite.

As also noted by previous studies (*e.g.*, Morata and Aguirre, 2003; Richards *et al*., 2017), trace elements distribution (here normalized to Primitive Mantle of Sun and McDonough, 1989) are the typical for magmas originated in subduction-related margins, with enrichment in LILE (Large Ion Lithophile Elements) relative to HFSE (High Field Strength Elements), Nb-Ta, Ti and P negative anomalies and positive Pb (Fig. 6A). Early Cretaceous lavas of Punta del Cobre Formation show the most primitive compositions in the studied section, but do not represent primary mantle melts, as suggested by low MgO contents in the andesites (most samples <4 wt%). However, the data of Morata and Aguirre (2003) for the upper section of the Punta del Cobre Formation (considered as Arqueros Formation by these authors) display relatively higher Th and U contents with respect to our data. These authors and Richards *et al*. (2017) also note the presence of Early Cretaceous samples with primary alkaline composition, not clearly distinguished in our analyses. Our data also reflect differences with composition of Early Cretaceous volcanic rocks described in detail by Marschik and Fontboté (2001) for the Punta del Cobre district at 27°30' S, where they report compositions between basalts and dacites for this unit and a slight enrichment in Zr/TiO_2 ratios with respect to our data. REE patterns tends to be similar for all volcanic units as normalized relative to Chondrite (Nakamura, 1974), with the higher REE contents in the upper member of the Cerrillos Formation. Most REE patterns of volcanic rocks are nearly flat and Eu negative anomalies are slightly marked in all units, including dacite porphyries. La/Sm increases toward younger units, whereas La_N/Yb_N values show a slight increase in Late Cretaceous dacite pophyries and Viñita Formation (Fig. 7A). The Sr contents are largely scattered in all sample groups, varying largely around 100 and 700 ppm, whereas Sr/Y ratios are mostly below 30 in all groups, as typical for arc magmas (Fig. 7B and C). The HFSE (High Field Strength Elements), especially Zr, Y and Nb, as well as Nb/Ta, Th/Ta and Ce/Pb ratios, are slightly increased for samples of

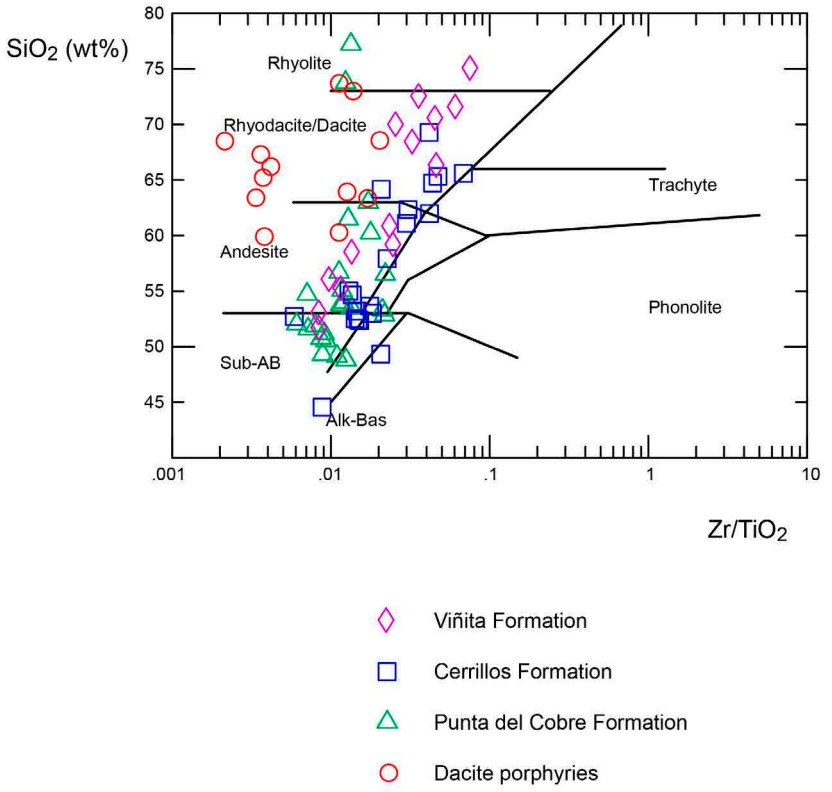

FIG. 5. Rock classification diagram (SiO_2 wt% *versus* Zr/TiO_2, Winchester and Floyd, 1977) for Cretaceous volcanic rocks, including samples from the Punta del Cobre, Bandurrias, Cerrillos and Viñita formations, and lower and upper Cretaceous Cu-bearing porphyry intrusions. **Sub-AB:** Sub-alkaline basalt; **Alk-Bas:** Alkaline basalt.

the upper member of the Cerrillos Formation and some dacite porphyries (Fig. 7D).

6. Discussion

6.1. Major tectonic events during the Early to Late Cretaceous

Field evidences obtained in this study allowed to detect two major transpressive/compressive tectonic events that disrupt relative dominant extensional conditions prevalent in the overriding plate during at least the Early Cretaceous (*i.e.*, Aberg *et al*., 1984; Mpodozis and Ramos, 1989; Lucassen *et al*., 2006, among others). The nature of the evidences of these events are dependent on their paleogeographic domain, since in the Lower Cretaceous magmatic arc domain, current Coastal Range, these correspond to ductile deformation zones related to the emplacement of Early Cretaceous plutonic complexes and lava sequences (*i.e.*, Arévalo and Welkner, 2008; Arévalo *et al*., 2009), while farther east, in the Cretaceous back-arc basin domain, these events are recorded as unconformities, crosscutting relationships with faults and sedimentary provenance indicators as demonstrated in this study. Our interpretation is in part contradictory with that of Richards *et al*. (2017), who proposed that the Cretaceous arc/backarc developed in three separated stages: >125 Ma extension, 125-110 Ma back-arc extension and rifting and 110 Ma and younger contraction.

The first identified tectonic deformation event detected along the studied segment is recorded in the magmatic arc domain and corresponds to left-lateral transpressive deformation registered along major segments of the Atacama Fault System (AFS). These segments are represented by Las Leñas, El Tofo, La Higuera and Algarrobo faults (Arévalo and Creixell, 2009). While El Tofo and Algarrobo faults display pure left-lateral displacement observed in cataclasites

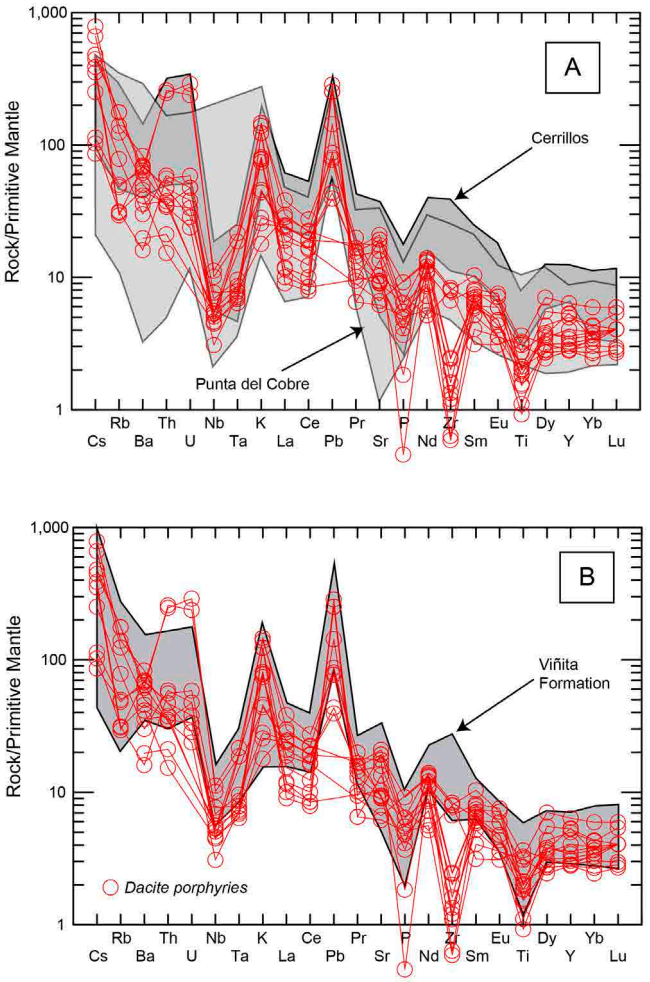

FIG. 6. Whole-rock trace elements distribution (spider diagram) normalized on the Primitive Mantle composition of Sun and McDonough (1989). In **A.** The Lower and Upper Cretaceous porphyries (red open circles) are compared with composition of the Punta del Cobre and Cerrillos formations volcanic rocks; **B.** Cretaceous porphyries (red open circles) compared to Upper Cretaceous Viñita Formation.

and mylonites, the La Higuera fault exhibits ductile vertical displacements along S-C shear zones and evidenced in sigmoidal porphyroclasts in mylonites from the margin of the El Trapiche Plutonic Complex. According to Arévalo and Creixell (2009) and Creixell *et al.* (2012), these faults, together with subsidiary faults that host hydrothermal IOCG deposits configure a whole left-lateral transpressional field that started around 121 Ma. All these ductile and brittle faults that are recognized along the Early Cretaceous arc domain have direct spatial relationship with magmatic rocks and alteration zones dated between 121 and 117 Ma, and show an overprint by alteration zones dated around 110 Ma (Creixell *et al*., 2012). In the back-arc domain, the Early Cretaceous deformation is recorded as an angular and erosional unconformity between the Pabellón and Cerrillos formations that, according to stratigraphic and geochronological data, represent a tectonic deformation event occurred between 116 and 110 Ma (Creixell *et al*., 2013). This unconformity represents a major change of marine to continental conditions of sedimentation, reflected by the shift from marine carbonate precipitation to siliciclastic deposition, and, consequently, the onset of subaerial drainage systems. These data suggest that the Early Cretaceous deformation front migrated from

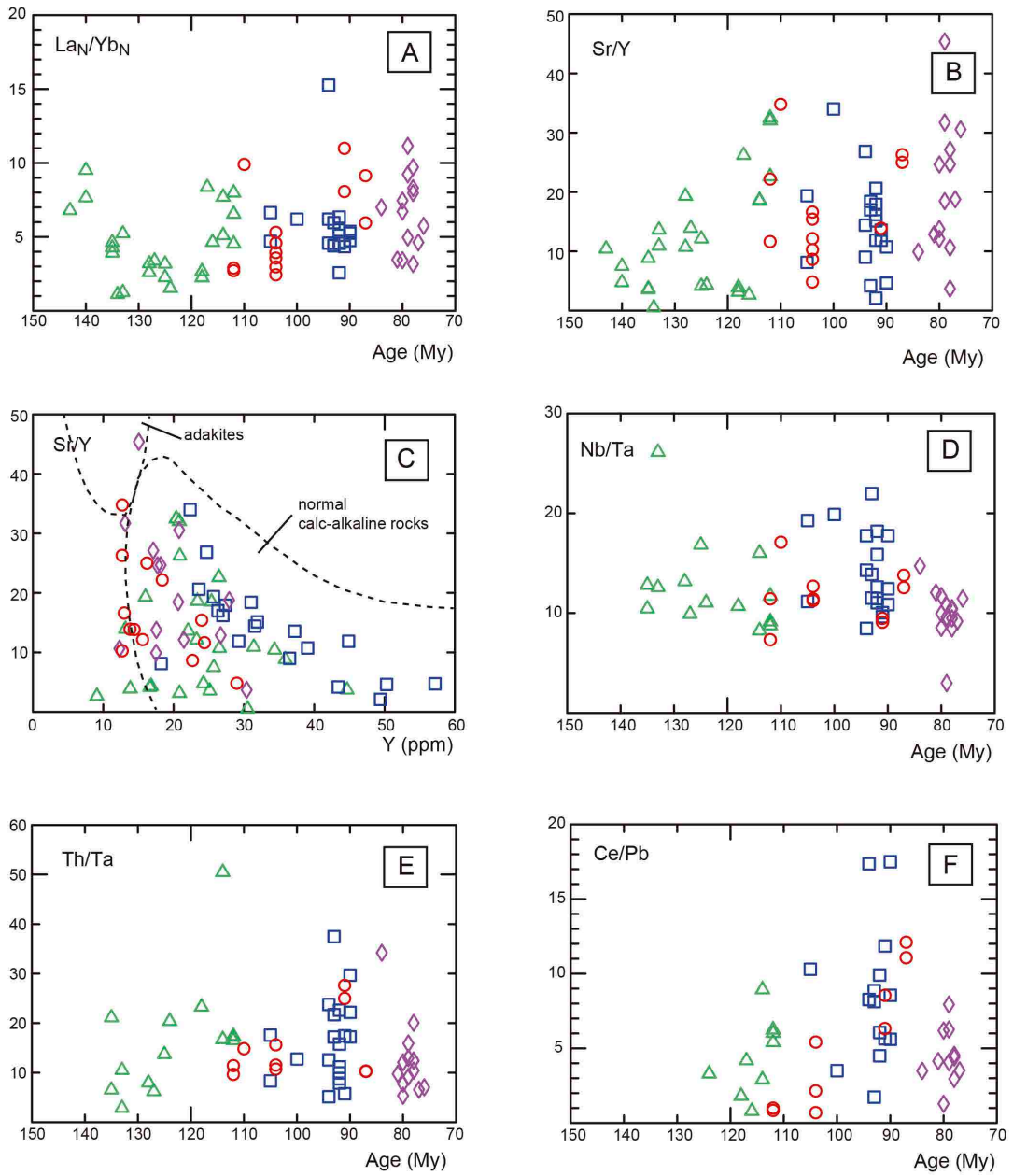

FIG. 7. Geochemical bivariant diagrams for whole-rock composition of Cretaceous volcanic rocks and porphyry intrusives. **A.** La_N/Yb_N (normalized to C1-Chondrite of Nakamura, 1974), *versus* Age (My=million years); **B.** Sr/Y ratios *versus* Age; **C.** Sr/Y ratios *versus* Y contents in ppm. Compositional fields after Defant and Drummond (1990); **D.** Nb/Ta ratios *versus* Age; **E.** Th/Ta *versus* Age; **F.** Ce/Pb ratios *versus* Age. Symbols legend as in figure 5.

west to east after 117 Ma, following a progressive migration of the volcanic front in the same direction (Punta del Cobre to Cerrillos formations). The character of the deformation probably changed in time from sinistral transpressive deformation along the arc to east-west compressive one in the eastern back-arc

domain. After the transpression ceased in the arc at 117 Ma and moved to the back-arc, both areas were ubiquitously invaded by magmas and hydrothermal fluids between 116 and 110 Ma, as is registered by the dacite and diorite intrusives related to porphyry copper-like mineralization, and dike swarms that crosscut older alteration zones related to IOCG and IOA deposits (Travisany *et al*., 1995; Creixell *et al*., 2012). With these data we can establish that the first episode of Cu-bearing dacite porphyry intrusions took place during this tectonic deformation event, and not during an extensional/transtensional event, as proposed by Richards *et al.* (2017) for north Chile. The whole Early Cretaceous tectonic event registered here between 121 and 110 Ma can be correlated with the first stage of development of the Mochica Deformation Event, well documented in the Peruvian Andes (Jaillard, 1994; Jaillard and Soler, 1996).

The second relevant tectonic deformation event has been recognized only along the eastern part of the segment considered in this study, where folding and faulting of the Chañarcillo Group in the north, and Cerrillos Formation to the south, is recognized along the Las Cañas-El Torito Fault (LCETF in Fig. 1). As described in previous sections, deformation corresponds to the overthrusting of the Chañarcillo Group limestones above the Cerrillos Formation volcanic rocks. Also, a large unconformity surface, recognized along the contact between the rocks of the Cerrillos and overlying Viñita formations, is observed in the study area. A large portion of the stratigraphy of the Cretaceous rock sequence is also repeated along this fault, but this displacement diminished towards south, disappearing almost completely around 30° S. The geological data (Creixell *et al*., 2013; Salazar *et al*., 2013) indicates that the deformation took place between 89 and 84 Ma mostly along the LCETF, accompanied by migration of the magmatic foci to the east. As we note that three Cu-bearing dacite porphyries occur close to the fault in time and space, we can hypothesize that this Late Cretaceous tectonic deformation event excerted control on the localization of these Cu-bearing porphyries. At a broad scale, this Late Cretaceous compressive event coincides with the early pulse of the Peruvian compressive phase highlighted by several authors (*e.g.*, Jaillard, 1992; Haschke *et al.*, 2002). In the eastern margin of the Cretaceous intraarc basin, provenance studies with detrital zircon U-Pb ages on the Pucalume Formation sedimentary rocks, evidence denudation of an uplifted eastern Permian (Cisuralian) basement block between 91 and 80 Ma (Merino *et al.*, 2013). Such basement block is very well constrained through regional mapping and corresponds mostly to Early Permian plutonic complexes, bounded by the San Félix and Pinte reverse faults in the eastern part of the studied area (Salazar *et al.*, 2013). The latter shows that the Late Cretaceous compressive deformation event at this latitude was spread into the foreland and that it involved basement blocks. The regional importance of the Late Cretaceous "Peruvian" compressive event in the margin of the southern central Andes has been highlighted by several authors (*e.g.*, Jaillard, 1992; Mescua *et al.*, 2013; Bascuñan *et al.*, 2015), as the start of the continuous compressive conditions of the margin until the present times.

6.2. Tectonic significance of compositional trends in magmatism

A remarkable feature of Cretaceous magmatic rocks in the study area is the tendency to more evolved composition through time, from dominantly basaltic andesites in Lower Cretaceous rocks to andesite and dacites in Upper Cretaceous.

Several studies has pointed out that porphyry copper deposits are derived from magmatic suites, largely oxidized and enriched in sulphur but most importantly in water (*e.g.*, Richards, 2011, and references therein). A relevant feature detected in this study is that the suite of Early Cretaceous dacite intrusions has indications of having been derived from differentiated magmas (compared to volcanic rocks) that were also richer in water (>4 wt% H_2O in the magma, Ridolfi *et al.*, 2010) as indicated by the persistent presence of amphibole as phenocryst in these rocks (Fig. 3C). Recent work by Richards *et al.* (2017) confirms that the studied Cretaceous Cu-porphyries are comparatively richer in S than Early Cretaceous IOCG deposits. On the other hand, some studies have noted that a direct relationship between porphyry copper genesis and stages of crustal shortening can be envisaged, especially for the Cenozoic Andean environment where a correlation between large deformation events and geochemical changes in magma composition have been detected (Kay and Mpodozis, 2001; Bissig *et al.*, 2003; Rabbia *et al*., 2003; Mpodozis and Cornejo, 2012).

As suggested by some compositional characteristics such as LILE enrichment over HFSE, Nb-Ta

depletion, Pb enrichment and Sr/Y<30, the magmas that originated the Cretaceous volcanic rocks show typical geochemical features for magmas generated in a subduction-related active margin. In general terms, REE patterns are flat, with (La_N/Yb_N) ratios <10. These values suggest an origin from melting of a depleted mantle-derived magma, with minor involvement of crustal component in their genesis (*e.g.*, Pearce, 1982). However, variable but intermediate #mg values between 25 and 50 indicate that magmas were not primary mantle melts, but fractionated or differentiated after melting from a possible mantelic source (*e.g.*, Klein and Langmuir, 1987). This is consistent with previous interpretations for the Cretaceous magmatism based on trace elements and Sr-Nd isotopic ratios that suggest that an origin from mantle melts modified in low degree by crustal melts and more shallow processes such as magma differentiation (*e.g.*, Vergara *et al.*, 1995; Morata and Aguirre, 2003). Richards *et al.* (2017) note that the Early Cretaceous (125-110 Ma) igneous rocks from north Chile show a primitive isotopic composition (higher εNd values towards N-MORB), that is consistent with our major and trace elements data that suggest that the Punta del Cobre lavas are the least differentiated in composition. The lack of a strongly marked Eu anomalies (Eu/Eu*<0.2; Fig. 6) suggest moderate to high O_2 fugacity of the magma or plagioclase fractionation (*e.g.*, Burnham *et al.*, 2015).

When compared with the older volcanics of the Punta del Cobre Formation and from the lower member of the Cerrillos Formation, the volcanic rocks of the upper member of this last unit display some minor geochemical changes, by example an increase in Th/Ta ratios (Fig. 7E), that can be interpreted as an increase in crustal contamination (*e.g.*, Condie, 2003) around the 89-92 Ma period, coincident with the onset of the Peruvian deformation stage. Similarly, Ce/Pb, Th/La and Nb/Ta ratios also show a slight increase around 90 Ma. The increase in these ratios and particularly the increase in Th, Ce and possibly Nb point out towards a modification of the primary mantle source by an external source like crustal fluids or slab-derived fluids (see by example Oliveros *et al.*, 2007). Isotopic data from Richards *et al.* (2017) show a slight scatter of Nd-Sr isotope ratios for Late Cretaceous igneous rocks that can be interpreted as a small degree of interaction between MORB-like and crustal sources.

In summary, our geochemical data point to subtle changes in trace elements ratios and magma sources as mentioned above around 90 Ma, but also only slight changes in, for example, La_N/Yb_N (Fig. 7A) or Sm/Yb ratios, so we can discard a major crustal thickening processes as responsible for these changes in geochemical composition around 90 Ma. The Yb values normalized to C1 chondrite (Sun and McDonough, 1989) over 10, exclude the presence of stable garnet in the source of magmas (*e.g.*, Gromet and Silver, 1987), and by consequence suggest that relevant crustal thickening (>40 km) during the Cretaceous and especially during the transpressive or compressional stages described above, was not present. In the same way, Sm/Yb for the more basic rocks are always low (<3), and according to Kay and Mpodozis (2001), such low values are indicative of a low pressure mantle source with clinopyroxene fractionation in the lower crust.

As a reference, we use the geochemical parameters of La/Yb or Sr/Y for estimation of crustal thickness during magma genesis (Chapman *et al.*, 2015; Profeta *et al.*, 2015) as these trace element ratios are largely controlled by crustal thickness in arc settings (see also Chiaradia, 2015). After filtering data to the restriction given by Profeta *et al.* (2015), we can note a two consecutive steplike increases in calculated crustal thicknesses from La/Yb ratios, from less than 30 km in Punta del Cobre Formation to around 40 km between 120 and 110 Ma, and from around 40 to more than 50 km between 80 and 90 Ma (Fig. 8), coincident with both, the Early Cretaceous transpressive event (120-110 Ma) and the Peruvian deformation (80-90 Ma),described in previous sections . Calculated thickness from Sr/Y give more disperse values, but still showing a tendency to increase around 90 Ma. Finally we can hypothesize that the Late Cretaceous compressive event, at least at the studied segment and domains, had a traceable imprint on the magma composition, but minor when compared with composition of Neogene magmatic rocks associated to major orogenic phases in the Eocene or Miocene (*e.g.*, Kay and Mpodozis, 2001; Haschke *et al.*, 2002; Bissig *et al.*, 2003).

6.3. Possible implications for mineral exploration of Cu resources.

The geochronological and geochemical data presented in this contribution points to a direct

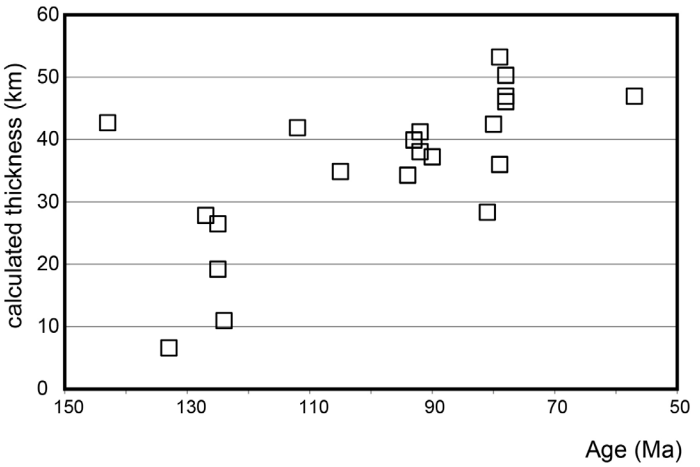

FIG. 8. Calculated thickness (crustal thickness in kilometers) *versus* Age of the rocks. Calculations using La/Yb ratios and data filtering, following Profeta *et al*. (2015).

relationship between the occurrence of porphyry copper deposits, porphyritic dacite intrusions and Cretaceous deformed belts, since most dacite porphyry and porphyry copper occurrences are restricted to a tectonic block limited by Cretaceous fault systems, the El Tofo Fault System by the west and the LCETF by the east. The older mineralization/alteration event is characterized by the occurrence of Cu-bearing dacite to diorite porphyritic intrusions with ages variable between 116 and 109 Ma, with a main cluster around 110-109 Ma and 106-104 Ma (Dos Amigos and Tricolor Cu-porphyries). These ages are also consistent with a prolongation of this belt to the south, considering the Andacollo mining district, dated at around 104 Ma (Maksaev *et al*., 2010; Richards *et al*., 2017). Most of these occurrences represent the relatively deep portion of Cu-porphyry systems, including the intrusive porphyries and locally potassic alteration zones. The westernmost of these intrusive porphyries (as dykes or stocks), are overimposed on the IOA and IOCG belts, generating complex patterns of alteration zones, with younger (110 Ma) alteration assemblages occurring close to older IOA- and IOCG-related alteration zones.

In the case of Late Cretaceous porphyry intrusions, its distribution is clearly limited to the east by the LCETF. These porphyries also show a close temporal and spatial relationship with the volcanic country rocks of the Cerrillos Formation and the location of the Chañarcillo Group marine deposits. This suggests that these mineralized intrusions are intimately linked with the host volcanic rocks, probably as hypabyssal intrusions. Therefore, we can propose that both the magmatic and structural systems were active during the Late Cretaceous. Furthermore, we can suggest the Late Cretaceous volcanic belt of the Upper Cerrillos Formation (dated between 92 and 88 Ma) as a first order control on the distribution on the Late Cretaceous porphyritic intrusions. At regional scale, the period of emplacement of the Late Cretaceous, Cu-bearing, dacite porphyry intrusions was coeval with the Peruvian orogenic phase, that in the study area, registered compressional deformation, with a subtle, but detectable change in the magma composition with respect to Early Cretaceous magmatism.

7. Concluding Remarks

Two main episodes of emplacement of dacite to diorite porphyries with associated porphyry copper type deposits have been identified in north Chile between 28º00’ and 29º30’ S. These episodes took place during the Early Cretaceous (116 to 104 Ma) and the Late Cretaceous (92 to 87 Ma). These intrusive porphyries are distributed within a tectonic block limited to the west by the eastern segments of the Atacama Fault System (El Tofo Fault System) and to east by the Las Cañas-El Torito Fault. The emplacement of the Early Cretaceous porphyries was contemporaneous with sinistral transpressive deformation that started at 121 Ma in the arc domain and migrated eastward to the back-arc domain

until 111 Ma, when a regional-scale unconformity was produced between the Pabellón and Cerrillos formations. The Late Cretaceous intrusive porphyries were emplaced coetaneous with a compressive deformative phase that, in the study area, was shown as reverse displacements along the LCETF, but at regional-scale, is correlated with the Peruvian Orogenic Phase (Jaillard, 1992).

The integrated geological observations, together with geochemical data on the Cretaceous volcanism from the Early to the Late Cretaceous, indicates that both Early and Late Cretaceous transpressive to compressional deformation episodes were not significant in terms of changes in the genesis of the magmatism, but trace element ratios such as Th/Ta, Nb/Ta and La/Yb suggest that the Late Cretaceous event was related to an increase in crustal thickness with respect to the Early Cretaceous, but minor compared to major Cenozoic orogenic phases, at least along the arc to back-arc domain.

Our findings suggest that regional mapping of the Cretaceous structural systems can be used as a first-order guide to the exploration of porphyry copper deposits associated to the dacite/diorite porphyries.

Acknowledgements

Most of the field observations were made during development of geological cartography programs of SERNAGEOMIN, funded by FNDR Project Nº BIP30068454-0 and PNG Project (Plan Nacional de Geología). The authors wish to thank J. Bustamante for geochemical analyses and R. Tello and H. Neira for their assistance in the field. We thank valuable comments on this paper by V. Maksaev and F. Henríquez. T. Bissig also made suggestions on a previous version of the manuscript. This work is part of the Postgraduate Thesis of the second author (J. Fuentes), and he wishes to thanks to the Postgraduate Program in Economic Geology from Universidad Católica del Norte.

References

Aberg, G.; Aguirre, L.; Levi, B.; Nyström, J. 1984. Spreading-subsidence and generation of ensialic marginal basins: an example from the Early Cretaceous of central Chile. Geological Society of London, Special Publication 16: 185-193.

Arancibia, G. 2004. Mid-cretaceous crustal shortening: evidence from a regional-scale ductile shear zone in the Coastal Range of central Chile (328° S). Journal of South American Earth Sciences 17: 209-226.

Arévalo, C.; Mourgues, F.A.; Chávez, R. 2009. Geología del área Vallenar-Domeyko. Región de Atacama. Servicio Nacional de Geología y Minería, Carta Geológica de Chile, Serie Geología Básica 120: 64 p., 1 mapa escala 1:100.000. Santiago.

Arévalo, C.; Creixell, C. 2009. The Atacama Fault System and its role on the migration and deposition of Iron Oxide Copper Gold and Magnetite-Apatite ores: an evaluation from the Los Choros and Huasco valleys. *In* Colloquium on Latin American Geosciences 21: 23-25. Germany.

Arévalo, C.; Welkner, D. 2008. Carta Carrizal Bajo-Chacritas, Región de Atacama. Servicio Nacional de Geología y Minería, Carta Geológica de Chile, Serie Geología Básica 111: 67 p., 1 mapa escala 1:100.000. Santiago.

Arredondo, C.; Prieto, X.; Mateo, L.; Ortega, R.; Ercilla, O.; Ulloa, M. 2018. Distritos y yacimientos metalíferos de la región de Coquimbo. Servicio Nacional de Geología y Minería, Boletín 65: 160 p.

Arriagada, C.; Cobbold, P.; Roperch, P. 2006. Salar de Atacama Basin: a record of compressional tectonics in the central Andes since the mid-Cretaceous. Tectonics 25 (1): 17-35.

Bascuñan, S.; Arriagada, C.; Le Roux, J.; Deckart, K. 2015. Unraveling the Peruvian Phase of the Central Andes: stratigraphy, sedimentology and geochronology of the Salar de Atacama Basin (22°30-23°S), northern Chile. Basin Research 28 (3): 365-392.

Bissig, T.; Clark, A.; Lee, J.; Von Quadt, A. 2003. Petrogenetic and metallogenetic responses to Miocene slab flattening: new constraints from the El Indio-Pascua Au-Ag-Cu belt, Chile/Argentina. Mineralium Deposita 38: 844-862.

Bookstrom, A.A. 1977. The magnetite deposits of El Romeral, Chile. Economic Geology 72: 1101-1130.

Boyce, D.; Charrier, R.; Farías, M. 2020. The first Andean compressive phase: Sedimentological and structural analysis of Mid-Cretaceous deposits in the Coastal Cordillera, central Chile (32°50' S). Tectonics 39. doi: 10.1029/2019TC005825.

Boric, R.; Diaz, F.; Maksaev, V. 1990. Geología y yacimientos metalíferos de la región de Antofagasta. Servicio Nacional de Geología y Minería, Boletín 40: 246 p.

Burnham, A.D.; Berry, A.J.; Halse, H.R.; Schofield, P.F.; Cibin, G.; Mosselmans, J.F.W. 2015. The oxidation state of europium in silicate melts as a function of oxygen fugacity, composition and temperature. Chemical Geology 411: 248-259.

Camus, F. 2003. Geología de los sistemas porfíricos en los Andes de Chile. Servicio Nacional de Geología y Minería: 267 p.

Chapman, J.; Ducea, M.N.; DeCelles, P.; Profeta, L. 2015. Tracking changes in crustal thickness during orogenic evolution with Sr/Y: An example from the North American Cordillera. Geology 43: 919-923.

Chiaradia, M. 2015. Crustal thickness control on Sr/Y signatures of recent arc magmas: an Earth scale perspective. Scientific Reports 5 (8115): 1-5.

Creixell, C.; Parada, M.A.; Morata, D.; Vásquez, P.; Pérez de Arce, C.; Arriagada, C. 2011. Middle-Late Jurassic to Early Cretaceous transtension and transpression during arc building in central Chile: evidence from mafic dike swarms. Andean Geology 38 (1): 37-63. doi: 10.5027/andgeoV38n1-a04.

Creixell, C.; Ortiz, M.; Arévalo, C. 2012. Geología del área Carrizalillo-El Tofo. Servicio Nacional de Geología y Minería, Carta Geológica de Chile, Serie Geología Básica 133-134: 82 p., 1 mapa escala 1:100.000. Santiago.

Creixell, C.; Labbé, M.; Arévalo, C.; Salazar, E. 2013. Geología del área Estación Chañar-Junta de Chingoles. Servicio Nacional de Geología y Minería, Carta Geológica de Chile, Serie Geología Básica 150: 85 p., 1 mapa escala 1:100.000. Santiago.

Creixell, C.; Fuentes, J.; Bierma, H.; Salazar, E. 2015. Tectónica regional y metalogénesis asociada al emplazamiento de la franja de pórfidos cupríferos cretácicos del norte de Chile (28°-30° S). *In* Congreso Geológico Chileno No. 14, Extended abstracts: 5 p. La Serena.

Cobbold, P.; Rosello, E. 2003. Aptian to Recent compressional deformation, foothills of the Neuquén basin, Argentina. Marine and Petroleum Geology 20: 429-443.

Condie, K. 2003. Incompatible element ratios in oceanic basalts and komatiites: Tracking deep mantle sources and continental growth rates with time. Geochemistry, Geophysics, Geosystems 4 (1): 1-28.

Coutand, I.; Cobbold, P.; Urreiztieta, M.; Gautier, P.; Chauvin, A.; Gapais, D.; Rosello, E.; López-Gamundi, O. 2001. Style and history of Andean deformation, Puna plateau, northwestern Argentina. Tectonics 20: 210-234.

Dallmeyer, R.D.; Brown, M.; Grocott, J.; Taylor, G.K.; Treolar, P.J. 1996. Mesozoic magmatic and tectonic events within the Andean plate boundary zone, 26°-27°30′ S, North Chile: constraints from $^{40}Ar/^{39}Ar$ mineral ages. Journal of Geology 104:19-40.

Defant, M.J.; Drummond, M.S. 1990. Derivation of some modern arc magmas by melting of young subducted lithosphere. Nature 347: 662-665.

Gana, P.; Zentilli, M. 2000. Historia termal y exhumación de intrusivos de la Cordillera de la Costa en Chile central: *In* Congreso Geológico Chileno, No. 9, Actas 2: 664-668. Puerto Varas.

García, F. 1967. Geología del Norte Grande de Chile. Sociedad Geológica de Chile, Simposio sobre el geosinclinal andino 3: 138 p. Santiago.

Gradstein, F.M.; Ogg, J.G.; Schmitz, M.D.; Ogg, G.M. (editores) 2012. The geologic time scale 2012. Elsevier: 1176 p. Boston.

Grocott, J.; Taylor, G. 2002. Deformation partitioning, magmatic arc fault systems and emplacement of granitic complex in the Coastal Cordillera, north Chilean Andes (25º30' to 27º00'S). Journal of the Geological Society of London 159: 425-442.

Gromet, L.P.; Silver, L.T. 1987. REE variations across the Peninsular Ranges Batholith; implications for batholithic petrogenesis and crustal growth in magmatic arcs. Journal of Petrology 28: 75-125.

Haschke, M.; Scheuber, E.; Günther, A.; Reutter, K-J. 2002. Evolutionary cycles during the Andean Orogeny: repeated slab breakoff and flat subduction? Terra Nova 14 (1): 49-55.

Jaillard, E. 1992. La Fase Peruana (Cretáceo Superior) en la Margen Peruana. Boletin de la Sociedad Geológica del Perú 83: 81-87.

Jaillard, E. 1994. Kimmeridgian to Paleocene tectonic and geodynamic evolution of the Peruvian 7and Ecuadorian Margin. *In* Cretaceous tectonics of the Andes (Salfity, J.; editor). Earth Evolution Sciences International Monograph Series, Wiesbaden:101-167.

Jaillard, E.; Soler, P. 1996. Cretaceous to early Paleogene tectonic evolution of the northern Central Andes (0-18°S) and its relations to geodynamics. Tectonophysics 259: 41-53.

Kay, S.M.; Mpodozis, C. 2001. Central Andean ore deposits linked to evolving shallow subduction systems and thickening crust. GSA Today 11 (3): 4-9.

Klein, E.; Langmuir, C. 1987. Global correlations of ocean ridge basalt chemistry with axial depth and crustal thickness. Journal of Geophysical Research 92: 8089-8115.

Knipping, J.L.; Bilenker, L.D.; Simon, A.C.; Reich, M.; Barra, F.; Deditius, A.P.; Lundstrom, C.; Bindeman, I.; Munizaga, R. 2015. Giant Kiruna-type deposits form by efficient flotation of magmatic magnetite suspensions. Geology 43 (7): 591-594.

Kloppenburg, A.; Grocott, J.; Hutchinson, D. 2010. Structural setting and synplutonic fault kinematics of a Cordilleran Cu-Au-Mo porphyry mineralization

system, Bingham mining district, Utah. Economic Geology 105: 743-761.

Levi, B.; Aguirre, L.; Nyström, J.O.; Padilla, H. 1989. Low-grade regional metamorphism in the Mesozoic-Cenozoic volcanic sequences of the Central Andes. Journal of Metamorphic Geology 7:487-495.

Llaumet, C. 1975. Faja Pacífica de cobres porfídicos y desarrollos de alteración hidrotermal en Chile. *In* Congreso Iberoamericano de Geología Económica, No. 2: 331-348. Buenos Aires.

Lucassen, F.; Kramer, W.; Bartsch, V.; Wilke, H-G.; Franz, G.; Romer, R.; Dulski, P. 2006. Nd, Pb, and Sr isotope composition of juvenile magmatism in the Mesozoic large magmatic province of northern Chile (18-27º S): indications for a uniform subarc mantle. Contributions to Mineralogy and Petrology 152: 571-589.

Maksaev, V.; Townley, B.; Palacios, C.; Camus, F. 2007. Metallic Ore Deposits. *In* The Geology of Chile (Moreno, T.; Gibbons, W.; editors). The Geological Society, Special Publication: 179-200. London.

Maksaev, V.; Munizaga, F.; Valencia, V.; Barra, F. 2009. LA-ICP-MS zircon U-Pb geochronology to constrain the age of post-Neocomian continental deposits of the Cerrillos Formation, Atacama Region, northern Chile: tectonic and metallogenic implications. Andean Geology 36 (2): 264-287. doi: 10.5027/andgeoV36n2-a05.

Maksaev, V.; Almonacid, T.; Munizaga, F.; Valencia, V.; McWilliams, M.; Barra, F. 2010. Geochronological and thermochronological constraints on porphyry copper mineralization in the Domeyko alteration zone, northern Chile. Andean Geology 37 (1): 144-176. doi: 10.5027/andgeoV37n1-a07.

Maksaev, V.; Llaumet, C. 2015. Guia de Excursion El Pleito-Mina Dos Amigos. Colegio de Geologos de Chile, Sociedad Geologica de Chile, Congreso Geológico Chileno No. 14, Field Guide: 13 p. La Serena.

Marschik, R.; Fontboté, L. 2001. The Punta del Cobre Formation, Punta del Cobre-Candelaria area, northern Chile. Journal of South American Earth Sciences 14: 401-433.

Matthews, S.; Cornejo, P.; Riquelme, R. 2006. Carta Inca de Oro, Región de Atacama. Servicio Nacional de Geología y Minería, Carta Geológica de Chile, Serie Geología Básica 102: 79 p., 1 mapa escala 1:100.000. Santiago.

Ménard, J-J. 1995. Relationship between altered pyroxene diorite and the magnetite mineralization in the Chilean Iron belt, with emphasis on the Algarrobo iron deposits (Atacama region, Chile). Mineralium Deposita 30: 268-274.

Menegazzo, M.C.; Catuneanu, O.; Chang, H.K. 2016. The South American retroarc foreland system: The development of the Bauru basin in the back-bulge province. Marine and Petroleum Geology 73: 131-156.

Merino, R.; Salazar, E.; Mora-Franco, C.; Creixell, C.; Coloma, F.; Oliveros, V. 2013. Fluvial deposition and retro-arc volcanism in a Late Cretaceous foreland basin and the unroofing of the Early Cretaceous arc in the Chilean Frontal Cordillera at 28°30'S, Atacama Region. Bolletino di Geofisica teorica ed applicata 54: 237 p.

Mescua, J.; Giambiagi, L.; Ramos, V. 2013. Late Cretaceous uplift in the Malargüe fold-and-thrust belt (35º S), southern central Andes of Argentina and Chile. Andean Geology 40 (1): 102-116. doi: 10.5027/andgeoV40n1-a05.

Morata, D.; Aguirre, L. 2003. Extensional Lower Cretaceous volcanism in the Coastal Range (29°20'-30°S), Chile: Geochemistry and petrogenesis. Journal of South American Earth Sciences 16: 459-476.

Morelli, P. 2008. Estudio geológico del sistema de alteración hidrotermal de Pajonales, Provincia de Vallenar, Región de Atacama. Memoria de Título (Unpublished), University of Chile, Departamento de Geología: 44 p.

Mpodozis, C.; Ramos, V.A. 1989. The Andes of Chile and Argentina. Circum-Pacific Council for Energy and Mineral Resources Earth Sciences Series 11: 59-90.

Mpodozis, C.; Cornejo, P. 2012. Cenozoic Tectonics and Porphyry Copper Systems of the Chilean Andes. *In* Geology and genesis of major copper deposits and districts of the world: A tribute to Richard H. Sillitoe. Society of Economic Geologists (Hedenquist, J.; Harris, M.; Camus, F.; editors). Special Publications 16: 329-360. Littleton.

Nakamura, N. 1974. Determination of REE, Ba, Fe, Mg, Na and K in carbonaceous and ordinary chondrites. Geochimica and Cosmochimica, Acta 38: 757-775.

Nyström, J.O.; Henríquez, F. 1994. Magmatic features of iron ores of the Kiruna type in Chile and Sweden: Ore textures and magnetite geochemistry. Economic Geology 89: 820-839.

Oliveros, V.; Morata, D.; Aguirre, L.; Feraud, G.; Fornari, M. 2007. Jurassic to Early Cretaceous subduction-related magmatism in the Coastal Cordillera of northern Chile (18°30'-24°S): geochemistry and petrogenesis. Revista Geológica de Chile 34 (2): 209-232. doi: 10.5027/andgeoV34n2-a03.

Oliveros, V.; Labbé, M.; Rossel, P.; Charrier, R.; Encinas, A. 2012. Late Jurassic paleogeographic evolution of the Andean back-arc basin: new constrains from

the Lagunillas Formation, northern Chile (27º30′-28º30′ S). Journal of South American Earth Sciences 37: 25-40.

Oyarzún, R.; Márquez, A.; Lillo, J.; López, I.; Rivera, S. 2001. Giant versus small porphyry copper deposits of Cenozic age in northern Chile: Adakitic versus normal calc-alkaline magmatism. Mineralium Deposita 32: 794-798.

Pearce, J.A. 1982. Trace element characteristics of lavas from destructive plate boundaries. *In* Andesites: Orogenic Andesites and Related Rocks (Thorpe, R.S.; editor), John Wiley and Sons: 525-548. New York.

Pineda, G.; Emparán, C. 2006. Geología del área Vicuña-Pichasca, Región de Coquimbo. Servicio Nacional de Geología y Minería, Mapas Geológicos 97, 1 mapa escala 1:100.000. Santiago.

Piquer, J.; Cooke, D.R.; Chen, J.; Zhang, L. 2017. Synextensional Emplacement of Porphyry Cu-Mo and Epithermal Mineralization. The Zijisnshan District, Southeastern China. Economic Geology 112: 1055-1074.

Profeta, L.; Ducea, M.N.; Chapman, J.; Paterson, S.; Henríquez, S.; Kirsch, M.; Petrescu, L.; DeCelles, P. 2015. Quantifying crustal thickness over time in magmatic arcs. Nature, Science Report 5: 17786. doi: 10.1038/srep17786.

Rabbia, O.; Hernandez, L.; King, R.; López- Escobar, L. 2003. Discussion on ‘‘Giant versus small porphyry copper deposits of Cenozoic age in northern Chile: adakitic versus normal calc-alkaline magmatism’’ by Oyarzun *et al*. Mineralium Deposita 37 (8): 791-794.

Reich, M.; Parada, M.A.; Palacios, C.; Dietrich, A.; Schultz, F.; Lehmann, B. 2003. Adakite-like signature of late Miocene intrusions at the Los Pelambres giant porphyry copper deposit in the Andes of central Chile: Metallogenic implications. Mineralium Deposita 38: 876-885.

Reich, M.; Simon, A.; Deditius, A.; Barra, F.; Chryssoulis, S.; Lagas, G.; Tardani, D.; Knipping, J.; Bilenker, L.; Sánchez-Alfaro, P.; Roberts, M.; Munizaga, R. 2016. Trace element signature of pyrite from the Los Colorados Iron Oxide-Apatite (IOA) deposit, Chile: A missing link between Andean IOA and Iron Oxide Copper Gold systems? Economic Geology 111 (3): 743-761.

Reyes, M. 1991. The Andacollo strata-bound gold deposit, Chile, and its position in a porphyry-gold system. Economic Geology 86: 1301-1316.

Richards, J. 2009. Post-subduction porphyry Cu-Au and epithermal Au deposits: products of remelting of subduction-modified lithosphere. Geology 37: 247-250.

Richards, J. 2011. High Sr/Y arc magmas and porphyry Cu±Mo±Au deposits: Just add water. Economic Geology 106 (7): 1075-1081.

Richards, J.; López, G.; Zhu, J-J.; Creaser, R.; Locock, A.; Mumin, H. 2017. Contrasting tectonic settings and sulfur contents of magmas associated with Cretaceous porphyry Cu±Mo±Au and Intrusion-related Iron Oxide Cu-Au deposits in northern Chile. Economic Geology 112: 295-318.

Ridolfi, F.; Renzulli, A.; Puerini, M. 2010. Stability and chemical equilibrium of amphibole in calcalkaline magmas: an overview, new thermobarometric formulations and application to subduction-related volcanoes. Contributions to Mineralogy and Petrology 160: 45-66.

Ring, U.; Willner, A.; Layer, P.; Richter, P. 2012. Jurassic to Early Cretaceous postaccretional sinistral transpression in northcentral Chile (latitudes 31-32°S). Geological Magazine 149 (2): 208-220.

Ruiz, C. 1967. Discusión sobre el origen de los yacimientos de Hierro. Minerales, Instituto de Ingenieros de Mina de Chile, año 22 (96-97): 9-22.

Ruiz, C.; Ortíz, F.; Moraga, A.; Aguilar, A. 1968. Genesis of Chilean Iron Ore Deposits of Mesozoic Age. *In* International Geological Congress, No. 22 (7):. 323-338.

Salazar, E.; Coloma, F.; Creixell, C. 2013. Geología del área El Tránsito-Lagunillas, Región de Atacama. Servicio Nacional de Geología y Minería, Mapas Geológicos, 149, 1 mapa escala 1:100.000. Santiago.

Salazar, E.; Franco, C.; Creixell, C.; Merino, R.; Suárez, M. 2015. Albian to Santonian tectonic closure of the Andean marginal basin at 28°S: Sedimentological, geochronological and structural evidences. *In* Congreso Geológico Chileno, No. 14, Actas 1: 729-732. La Serena.

Sanchez, M.; McClay, K.; King, A.; Wijbrans, J. 2016. Cenozoic Crustal Extension and Its Relationship to Porphyry Cu-Au-(Mo) and Epithermal Au-(Ag) Mineralization in the Biga Peninsula, Northwestern Turkey. Society of Economic Geologists, Special Publication 19: 113-156.

Scheuber, E.; Bogdanic, T.; Jensen, A.; Reutter, K-J. 1994. Tectonic development of the north Chilean Andes in relation to plate convergence and magmatism since the Jurassic. *In* Tectonics of the southern central Andes (Reutter, K-J.; Scheuber, E.; Wigger, P.; editors): 121-139. Berlin.

Scheuber, E.; González, G. 1999. Tectonics of the Jurassic-Early Cretaceous magmatic arc of the north Chilean Coastal Cordillera (22º-26º S): a story of

crustal deformation along a convergent plate boundary. Tectonics 18: 895-910.

Segerstrom, K.; Parker, R. 1959. Cuadrángulo Cerrillos. Provincia de Atacama. Instituto de Investigaciones Geológicas, Carta Geológica de Chile 2: 33 p., 1 mapa escala 1:50.000. Santiago.

Segerstrom, K.; Ruiz, C. 1962. Cuadrángulo Copiapó, Provincia de Atacama. Instituto de Investigaciones Geológicas, Carta Geológica de Chile 6: 115 p., 1 mapa escala 1:50.000. Santiago.

Sillitoe, R. 1981. Regional aspects of the Andean porphyry copper belt in Chile and Argentina. Transactions of the Institute of Mines and Metallurgy, Section B (90): 815-836.

Sillitoe, R. 1991. Gold metallogeny of Chile-An Introduction. Economic Geology 86: 1187-1205.

Sillitoe, R. 1998. Major regional factors favoring large size, high hypogene grade, elevated gold content and supergene oxidation and enrichment of porphyry copper deposits. *In* Porphyry and hydrothermal copper and gold deposits: A global perspective (Porter, T.M.; editor): Australian Mineral Foundation: 21-34. Adelaide.

Sillitoe, R. 2003. Iron oxide-copper-gold deposits: An Andean view. Mineralium Deposita 38: 787-812.

Sillitoe, R.; Perelló, J. 2005. Andean copper province: tectonomagmatic settings, deposit types, metallogeny, exploration, and discovery. *In* Economic geology one hundredth anniversary volume (1905-2005), (Hedenquist, J.W.; Thompson, J.F.H.; Goldfarb, R.; Richards, J.; editors). Society of Economic Geologists: 845-890. Littleton.

Sun, S.; McDonough, W.F. 1989. Chemical and isotopic systematics of oceanic basalts; implications for mantle composition and processes. *In* Magmatism in the Ocean Basins, (Saunders, A.D.; Norry, J.M.; editors). Geological Society of London Special Publication 42: 313-345.

Travisany, V.; Henríquez, F.; Nyström, J.O. 1995. Magnetite lava flows in the Pleito-El Melón district of the Chilean Iron Belt. Economic Geology 90: 438-444.

Tunik, M.; Folguera, A.; Naipauer, M.; Pimentel, M.; Ramos, V. 2010. Early uplift and orogenic deformation in the Neuquén basin: Constraints on the Andean uplift from U-Pb and Hf isotopic data of detrital zircons. Tectonophysics 489: 258-273.

Veloso, E.; Cembrano, J.; Arancibia, G.; Heuser, G.; Neira, S.; Siña, A.; Garrido, I.; Vermeesch, P.; Selby, D. 2016. Tectono-metallogenetic evolution of the Fe-Cu deposit of Dominga, northern Chile. Mineralium Deposita 52: 595-620. doi: 10.1007/s00126-016-0682-8.

Vergara, M.; Levi, B.; Nyström, J.O.; Cancino, A. 1995. Jurassic and Early Cretaceous island arc volcanism, extension, and subsidence in the Coast Range of central Chile. Geological Society of America Bulletin 107: 1427-1440.

Vivallo, W.; Henríquez, F. 1998. Génesis común de los yacimientos estratoligados y vetiformes de cobre del Jurásico Medio a Superior en la Cordillera de la Costa, Región de Antofagasta, Chile. Revista Geológica de Chile 25: 199-228. doi: 10.5027/andgeoV25n2-a06.

Vivallo, W.; Díaz, A.; Jorquera, R. 2008. Yacimientos metalíferos de la región de Atacama. Servicio Nacional de Geología y Minería, Carta Geológica de Chile, Serie Recursos Minerales y Energéticos 27: 151 p., 1 mapa escala 1:500.000. Santiago.

Welkner, D.; Arévalo, C.; Godoy, E. 2006. Geología del área Freirina-El Morado, Región de Atacama. Carta Geológica de Chile, Serie Geología Básica 100: 50 p., 1 mapa escala 1:100.000. Santiago.

Winchester, J.A.; Floyd, P.A. 1977. Geochemical discrimination of different magma series and their differentiation products using immobile elements. Chemical Geology 20: 325-343.

Zhang, H.; Hou, Z. 2018. Metallogenesis within continental collision zones: Comparisons of modern collisional settings. Science China Earth Sciences 61: 1737-1760

Manuscript received: January 24, 2017; revised/accepted: February 14, 2020; available online: May 29, 2020.

Appendix

TABLE 1A. ANALYTICAL DATA FOR ZIRCON LA-ICPMS U-Pb AGE DETERMINATIONS OBTAINED IN THE UNIVERSITY OF TASMANIA, WITH EXCEPTION OF SAMPLES PLC-52 AND PLC-51, ANALYZED AT GEOCHRONOLOGY LABORATORY OF SERNAGEOMIN.

				Isotopic Ratios						Age (Ma)							
Analisis	U	Th	Pb	$^{206}Pb/^{238}U$	error	$^{208}Pb/^{232}Th$	error	$^{207}Pb/^{206}Pb$	error	$^{206}Pb/^{238}U$	error	$^{208}Pb/^{232}Th$	error	$^{207}Pb/^{206}Pb$	error	$^{206}Pb/^{238}U(a)$	error
MJC-81	ppm	ppm	ppm	ratio	1σ%	ratio	1σ%	ratio	1σ%	age	1σ%	age	1σ%	age	1σ%	age	1σ%
2012-621	159	115	4	0.01778	2.26%	0.0056	3.57%	0.0507	5.97%	114	3	113	4	229	138	113	3
2012-621	218	174	5	0.0179	1.94%	0.0056	2.73%	0.0527	6.01%	115	2	114	3	317	137	114	2
2012-621	118	62	3	0.0179	2.54%	0.0054	4.16%	0.0443	7.86%	114	3	108	4	-95	193	115	3
2012-621	128	77	3	0.0181	2.09%	0.0060	2.99%	0.0496	5.92%	116	2	120	4	175	138	115	2
2012-621	80	33	2	0.0181	2.51%	0.0060	4.70%	0.0480	6.92%	116	3	122	6	99	164	116	3
2012-621	116	53	2	0,018	2.41%	0.0056	4.16%	0.0490	6.94%	116	3	113	5	149	163	116	3
2012-621	163	100	4	-	2.42%	0.0054	4.31%	0.0514	8.12%	117	3	109	5	258	187	116	3
2012-621	110	76	3	0.0183	2.30%	0.0060	3.54%	0.0507	6.72%	117	3	120	4	229	155	117	3
2012-621	55	21	1	0.0185	3.84%	0.0057	6.92%	0.0597	10.13%	118	5	114	8	593	220	117	5
2012-621	132	96	3	0.0185	2.15%	0.0060	2.88%	0.0563	5.18%	118	3	122	4	464	115	117	3
2012-621	215	160	5	0.0183	3.33%	0.0055	5.16%	0.0450	7.88%	117	4	111	6	-54	192	117	4
2012-621	84	33	2	0.0186	2.83%	0.0059	4.86%	0.0522	7.90%	119	3	118	6	297	180	118	3
2012-621	138	105	3	0.0185	2.00%	0.0052	2.68%	0.0460	5.61%	118	2	105	3	-2	135	118	2
2012-621	171	101	4	0.0185	1.73%	0.0059	2.72%	0.0468	4.69%	118	2	120	3	41	112	118	2
2012-621	72	31	2	0.0186	3.29%	0.0069	5.64%	0.0499	10.34%	119	4	140	8	189	241	118	4
2012-621	207	189	5	0.0187	1.68%	0.0056	2.50%	0.0543	4.76%	119	2	113	3	383	107	118	2
2012-621	75	34	2	0.0188	2.70%	0.0053	4.73%	0.0548	8.27%	120	3	107	5	405	185	119	3
2012-621	146	77	3	0.0188	2.06%	0.0056	3.56%	0.0527	5.55%	120	2	113	4	316	126	119	2
2012-621	72	36	2	0.0188	2.60%	0.0061	4.54%	0.0534	7.56%	120	3	122	6	345	171	119	3
2012-621	51	23	1	0.0191	3.15%	0.0062	5.39%	0.0587	8.56%	122	4	125	7	555	187	120	4
2012-621	86	54	2	0.0188	2.38%	0.0058	4.16%	0.0474	7.58%	120	3	116	5	68	180	120	3
2012-621	81	36	2	0.0189	2.56%	0.0061	4.84%	0.0505	7.28%	121	3	123	6	220	168	121	3
2012-621	73	36	2	0.0189	2.67%	0.0062	4.32%	0.0461	8.37%	120	3	125	5	4	202	121	3
2012-621	90	40	2	0.0190	2.31%	0.0057	4.47%	0.0484	7.68%	121	3	114	5	120	181	121	3
2012-621	82	35	2	0.0192	2.55%	0.0062	4.52%	0.0492	6.86%	122	3	126	6	159	160	122	3
2012-621	127	58	3	0.0191	2.33%	0.0063	3.72%	0.0460	6.86%	122	3	126	5	1	165	122	3
2012-621	68	29	2	0.0192	2.71%	0.0061	4.90%	0.0490	7.35%	123	3	123	6	150	172	123	3
2012-621	42	16	1	0.0193	3.54%	0.0061	6.71%	0.0533	10.00%	123	4	123	8	344	226	123	4
2012-621	133	67	3	0.0193	1.90%	0.0062	3.08%	0.0524	5.30%	123	2	125	4	303	121	123	2
2012-621	132	117	3	0.0194	2.02%	0.0057	2.59%	0.0490	5.23%	124	2	116	3	150	123	124	3

Weighted Mean Age (Ma±2σ): 118.6±1.0

MSWD: 1.03

table 1A continued.

				Isotopic Ratios							Age (Ma)								
sample	U	Th	Pb	$^{207}Pb/^{235}U$	error	$^{206}Pb/^{238}U$	error	rhoc	$^{207}Pb/^{206}Pb$	error	$^{207}Pb/^{235}U$	error	$^{206}Pb/^{238}U$	error	$^{207}Pb/^{206}Pb$	error	$^{206}Pb/^{238}U$(a)	error	$^{207}Pb/^{206}Pb$ common
PLC-52	ppm	ppm	ppm	ratio	2σ	ratio	2σ		ratio	2σ	age	2σ	age	2σ	age		age	2σ	
PLC-52_1	378	232	129	0.1295	0.003	0.01928	0.00048	0.77958	0.04804	0.00082	123.7	2.8	123.1	3.1	105	36	123.2	3.0	0.8436
PLC-52_2	67	24	14	0.1308	0.0036	0.01968	0.00037	0.46596	0.0486	0.0012	124.9	3.2	125.6	2.4	136	48	125.6	2.4	0.8438
PLC-52_3	203	88	48	0.1299	0.0026	0.01947	0.00036	0.61037	0.04857	0.00079	124,0	2.4	124.3	2.2	127	33	124.3	2.3	0.8437
PLC-52_4	50	19	11	0.1314	0.0045	0.01999	0.00039	0.27937	0.0486	0.0016	125.1	4.0	127.7	2.4	100	58	127.6	2.5	0.8439
PLC-52_5	101	33	18	0.1272	0.003	0.01946	0.00036	0.54919	0.0475	0.001	121.4	2.7	124.2	2.2	94	42	124.4	2.3	0.8437
PLC-52_6	178	67	38	0.1327	0.0038	0.01922	0.00042	0.58292	0.0492	0.0011	126.1	3.4	122.7	2.7	157	44	122.6	2.7	0.8436
PLC-52_7	148	67	36	0.1295	0.003	0.01984	0.00038	0.61617	0.0483	0.00093	123.4	2.7	126.6	2.4	122	39	126.7	2.4	0.8438
PLC-52_8	106	38	23	0.1327	0.0036	0.01974	0.00043	0.57312	0.0488	0.0011	126.2	3.2	126.0	2.7	142	47	126.0	2.7	0.8438
PLC-52_9	91	28	16	0.1317	0.0033	0.0195	0.00037	0.50408	0.0489	0.0011	125.4	3.0	124.5	2.3	143	43	124.4	2.3	0.8437
PLC-52_10	69	24	14	0.1322	0.0038	0.01988	0.00036	0.34585	0.0491	0.0013	125.5	3.3	126.8	2.3	145	47	126.8	2.3	0.8438
PLC-52_11	155	64	36	0.1284	0.0028	0.01988	0.00036	0.64535	0.04781	0.00084	122.4	2.5	126.9	2.3	98	35	127.0	2.3	0.8438
PLC-52_12	64	21	12	0.1296	0.0047	0.01947	0.00041	0.055811	0.049	0.0016	122.2	3.8	124.3	2.6	115	57	124.2	2.6	0.8437
PLC-52_13	97	35	19	0.1312	0.0038	0.01969	0.00037	0.05898	0.0492	0.0012	124.6	3.4	125.6	2.3	142	45	125.6	2.3	0.8438
PLC-52_14	159	80	44	0.1278	0.0027	0.01996	0.00038	0.49041	0.04762	0.00091	121.7	2.4	127.3	2.4	93	35	127.6	2.4	0.8438
PLC-52_15	53	21	12	0.1282	0.004	0.01958	0.00039	0.40653	0.0483	0.0014	122.8	3.6	124.9	2.4	116	55	125.0	2.5	0.8437
PLC-52_16	111	54	31	0.1348	0.0039	0.01987	0.00043	0.23745	0.0495	0.0013	127.8	3.5	126.8	2.7	147	48	126.7	2.7	0.8438
PLC-52_17	156	77	45	0.1355	0.0031	0.02027	0.00039	0.54643	0.04805	0.0009	129,0	2.8	129.3	2.5	107	37	129.4	2.5	0.8440
PLC-52_18	65	21	13	0.1314	0.006	0.01927	0.00059	0.3173	0.0499	0.0021	124.6	5.4	123.0	3.7	157	78	122.8	3.8	0.8436
PLC-52_19	96	44	26	0.1351	0.0047	0.02073	0.00056	0.52532	0.0489	0.0015	129.1	4.3	132.2	3.5	142	63	132.2	3.6	0.8442
PLC-52_20	52	19	11	0.133	0.0046	0.02012	0.0004	0.33321	0.0488	0.0016	126.6	4.0	128.3	2.5	146	59	128.4	2.5	0.8444
PLC-52_21	63	24	13	0.1285	0.0041	0.01959	0.00038	0.34569	0.0488	0.0014	122.6	3.6	125.1	2.4	135	52	125.0	2.4	0.8437
PLC-52_22	108	60	35	0.1311	0.0035	0.01976	0.00043	0.61788	0.0488	0.0011	125.1	3.2	126.2	2.7	141	43	126.1	2.7	0.8438
PLC-52_23	52	22	13	0.1359	0.0046	0.02035	0.00042	0.35888	0.0492	0.0016	129.1	4.2	129.8	2.7	171	62	129.8	2.7	0.8440
PLC-52_24	49	19	11	0.1333	0.0048	0.02025	0.00039	0.25121	0.0484	0.0016	125.8	4.2	129.2	2.5	98	60	129.3	2.5	0.8440
PLC-52_25	46	16	9	0.1349	0.0045	0.01957	0.00041	0.343	0.0506	0.0016	128.1	4.0	124.9	2.6	195	61	124.6	2.6	0.8437
PLC-52_26	88	34	20	0.1318	0.004	0.01976	0.00045	0.37488	0.0496	0.0012	124.8	3.4	126.2	2.8	145	47	126.0	2.8	0.8438
PLC-52_27	47	16	9	0.1303	0.0049	0.01987	0.00041	0.40281	0.0487	0.0017	123.9	4.4	126.8	2.6	141	62	126.8	2.6	0.8438
PLC-52_28	65	24	13	0.132	0.0045	0.0198	0.00046	0.43063	0.0494	0.0015	125.8	4.0	126.3	2.9	170	60	126.2	2.9	0.8438
PLC-52_29	85	33	19	0.1302	0.0033	0.01963	0.00037	0.47712	0.0488	0.0011	124.2	3.0	125.3	2.4	139	44	125.3	2.4	0.8438
PLC-52_30	184	71	40	0.1295	0.003	0.01978	0.00044	0.46655	0.04828	0.00099	123.1	2.7	126.2	2.8	99	39	126.3	2.8	0.8438
PLC-52_31	54	17	10	0.1315	0.0046	0.01967	0.00046	0.29761	0.0498	0.0017	125.3	4.1	125.5	2.9	166	65	125.4	2.9	0.8438
PLC-52_32	127	44	25	0.1284	0.0033	0.01986	0.00041	0.5246	0.048	0.0011	122.7	2.9	126.7	2.6	108	44	126.9	2.6	0.8438
PLC-52_33	80	27	16	0.1323	0.0036	0.01939	0.00039	0.40479	0.0494	0.0013	125.7	3.2	123.8	2.4	169	50	123.7	2.5	0.8437
PLC-52_34	44	13	7	0.1361	0.0053	0.0198	0.00048	0.34098	0.0508	0.0019	128.6	4.7	126.3	3.1	206	67	126.0	3.0	0.8438
PLC-52_35	79	27	16	0.1335	0.0037	0.01998	0.0004	0.44732	0.0494	0.0012	126.7	3.3	127.5	2.5	164	49	127.4	2.5	0.8439
PLC-52_36	110	51	30	0.1336	0.0045	0.02029	0.00045	0.085755	0.0489	0.0013	125.6	3.7	129.4	2.9	116	49	129.4	2.8	0.8440
PLC-52_37	49	16	9	0.1371	0.0061	0.02071	0.00048	0.10868	0.0495	0.002	127.6	4.8	132.1	3.0	113	66	132.0	3.0	0.8442
PLC-52_38	75	27	16	0.1318	0.0056	0.01944	0.00059	0.34158	0.0486	0.0018	124.9	4.8	124.1	3.7	137	67	124.1	3.7	0.8437
PLC-52_39	33	14	8	0.1338	0.0058	0.01975	0.00044	0.2374	0.05	0.002	124.8	4.9	126.0	2.8	142	70	125.8	2.8	0.8438

table 1A continued.

				Isotopic Ratios							Age (Ma)								
sample	U	Th	Pb	$^{207}Pb/^{235}U$	error	$^{206}Pb/^{238}U$	error	rhoc	$^{207}Pb/^{206}Pb$	error	$^{207}Pb/^{235}U$	error	$^{206}Pb/^{238}U$	error	$^{207}Pb/^{206}Pb$	error	$^{206}Pb/^{238}U(a)$	error	$^{207}Pb/^{206}Pb$
PLC-52	ppm	ppm	ppm	ratio	2σ	ratio	2σ		ratio	2σ	age	2σ	age	2σ	age		age	2σ	common
PLC-52_40	64	23	13	0.1358	0.0044	0.01997	0.00043	0.40658	0.0496	0.0013	128.5	3.8	127.4	2.7	161	51	127.3	2.7	0.8439
PLC-52_41	38	14	8	0.1387	0.0051	0.01982	0.00042	0.31678	0.0516	0.0018	131.5	4.6	126.5	2.6	247	68	126.0	2.7	0.8438
PLC-52_42	160	76	44	0.1324	0.003	0.01973	0.00037	0.58457	0.04957	0.00096	125.9	2.7	125.9	2.3	159	37	125.8	2.3	0.8438
PLC-52_43	157	60	34	0.1254	0.003	0.01896	0.0004	0.58126	0.04826	0.00098	120.1	2.7	121.0	2.5	108	39	121.1	2.5	0.8435
PLC-52_44	77	38	22	0.1334	0.0044	0.01956	0.00042	0.008364	0.0507	0.0014	126.4	3.9	124.9	2.7	192	54	124.5	2.7	0.8437
PLC-52_45	283	146	84	0.1283	0.0026	0.01957	0.00038	0.70249	0.04811	0.00073	122.4	2.3	124.9	2.4	111	31	125.0	2.4	0.8437
PLC-52_46	199	99	61	0.1517	0.0047	0.02189	0.00072	0.69018	0.0494	0.0011	143.2	4.1	139.5	4.5	159	44	139.5	4.6	0.8447
PLC-52_47	99	64	37	0.1325	0.0038	0.01987	0.00041	0.31069	0.0501	0.0013	125.8	3.3	126.8	2.6	160	47	126.6	2.6	0.8438
PLC-52_48	117	49	28	0.1305	0.0035	0.01941	0.00042	0.61121	0.049	0.0011	124.1	3.2	123.9	2.7	153	45	123.8	2.7	0.8437
PLC-52_49	133	80	46	0.1303	0.0032	0.01987	0.00042	0.50032	0.048	0.001	124.1	2.9	126.7	2.7	120	42	126.9	2.7	0.8438
PLC-52_50	50	19	12	0.1397	0.0049	0.02035	0.00038	0.26304	0.05	0.0016	132.4	4.2	129.8	2.4	187	60	129.6	2.4	0.8440
PLC-52_51	55	19	11	0.1336	0.0048	0.01949	0.00036	0.25409	0.0496	0.0017	127.2	4.2	124.6	2.3	150	65	124.3	2.3	0.8437
PLC-52_52	83	32	19	0.1327	0.0035	0.01986	0.00038	0.28236	0.0484	0.0013	126.4	3.1	126.7	2.4	127	49	126.8	2.4	0.8438
PLC-52_53	173	87	46	0.1229	0.0027	0.01885	0.00034	0.48199	0.04776	0.0009	117.6	2.4	120.4	2.2	96	37	120.5	2.2	0.8434
PLC-52_54	66	42	24	0.1299	0.0039	0.01971	0.00035	0.32669	0.0476	0.0013	123.2	3.5	125.9	2.2	85	51	126.0	2.2	0.8438
PLC-52_55	128	69	40	0.1289	0.0031	0.01986	0.00037	0.45245	0.0476	0.001	122.7	2.8	126.7	2.3	89	41	126.9	2.3	0.8438
PLC-52_56	71	25	15	0.1326	0.0041	0.01951	0.00034	0.25139	0.0494	0.0014	125.7	3.6	124.7	2.1	138	52	124.4	2.2	0.8437
PLC-52_57	107	37	22	0.1302	0.0032	0.01961	0.00036	0.54411	0.0492	0.0011	124.1	2.9	125.2	2.3	157	43	125.1	2.3	0.8437
PLC-52_58	148	47	27	0.1287	0.0026	0.01963	0.00035	0.48301	0.04785	0.00088	123.1	2.3	125.3	2.2	103	36	125.4	2.2	0.8438
PLC-52_59	59	37	21	0.1289	0.0043	0.01995	0.00043	0.42055	0.0478	0.0015	122.7	3.9	127.3	2.7	124	59	127.5	2.7	0.8439
PLC-52_60	68	40	23	0.1327	0.0041	0.0197	0.0004	0.22127	0.0497	0.0015	125.9	3.7	125.7	2.5	157	52	125.6	2.6	0.8438
PLC-52_61	95	34	20	0.1325	0.0038	0.01976	0.00037	0.38834	0.0487	0.0012	126.1	3.3	126.1	2.4	127	49	126.1	2.4	0.8438
PLC-52_62	120	64	38	0.131	0.0031	0.01983	0.00038	0.45094	0.048	0.0011	124.7	2.8	126.5	2.4	109	43	126.7	2.4	0.8438
PLC-52_64	70	24	15	0.134	0.0039	0.01984	0.00039	0.39217	0.05	0.0014	128.0	3.4	126.6	2.4	186	52	126.4	2.5	0.8438
PLC-52_65	136	48	28	0.1276	0.0031	0.01972	0.00042	0.59784	0.04727	0.00093	121.8	2.8	125.8	2.7	79	38	126.1	2.7	0.8438
PLC-52_67	130	47	27	0.1297	0.0029	0.01991	0.00036	0.25159	0.04736	0.00095	123.7	2.6	127.1	2.3	77	39	127.3	2.3	0.8439
PLC-52_68	97	32	18	0.1296	0.0032	0.01958	0.00041	0.49938	0.0485	0.0011	124.3	2.9	124.9	2.6	135	45	125.0	2.6	0.8437
PLC-52_69	54	19	11	0.1304	0.0065	0.02084	0.00064	0.43004	0.0475	0.0022	124.7	5.9	132.9	4.1	76	85	133.2	4.1	0.8442
PLC-52_70	95	40	23	0.1292	0.0034	0.02014	0.00046	0.52756	0.0479	0.0012	123.2	3.1	128.5	2.9	106	50	128.6	2.9	0.8440
PLC-52_71	232	117	65	0.1292	0.0025	0.01953	0.00033	0.62877	0.04822	0.00078	123.4	2.3	124.6	2.1	116	33	124.7	2.1	0.8437
PLC-52_72	80	26	16	0.1368	0.0039	0.02045	0.00042	0.38234	0.0493	0.0013	129.8	3.4	130.5	2.7	141	49	130.4	2.7	0.8441
PLC-52_73	133	61	35	0.1328	0.0031	0.0198	0.0004	0.54599	0.0493	0.0011	126.6	2.8	126.4	2.5	164	42	126.3	2.5	0.8438
PLC-52_74	145	55	33	0.1326	0.0031	0.02006	0.00037	0.50888	0.04782	0.00096	126.1	2.8	128.0	2.3	98	39	128.2	2.3	0.8439
PLC-52_75	277	217	127	0.1428	0.0047	0.01963	0.0004	0.52197	0.0535	0.0014	135.0	3.9	125.2	2.5	287	47	124.5	2.5	0.8437
PLC-52_76	106	38	22	0.1323	0.0035	0.01957	0.00038	0.45887	0.0498	0.0011	126.1	3.1	124.9	2.4	176	43	124.7	2.4	0.8437
PLC-52_77	182	88	56	0.1399	0.0057	0.01872	0.00063	0.4523	0.0523	0.0019	132.6	5.1	119.5	4.0	269	74	119.0	4.0	0.8434
PLC-52_78	85	35	21	0.1301	0.0037	0.02008	0.00042	0.378	0.0481	0.0013	123.8	3.3	128.1	2.6	106	50	128.2	2.7	0.8439

Weighted Mean age (Ma±2σ): 126.1±0.1

MSWD: 1.7

table 1A continued.

				Isotopic Ratios							Age (Ma)								
sample	U	Th	Pb	$^{207}Pb/^{235}U$	error	$^{206}Pb/^{238}U$	error	rhoc	$^{207}Pb/^{206}Pb$	error	$^{207}Pb/^{235}U$	error	$^{206}Pb/^{238}U$	error	$^{207}Pb/^{206}Pb$	error	$^{206}Pb/^{238}U(a)$	error	$^{207}Pb/^{206}Pb$
PLC-51	ppm	ppm	ppm	ratio	2σ	ratio	2σ		ratio	2σ	age	2σ	age	2σ	age		age	2σ	common
PLC-51_1	164	73	38	0.1201	0.0026	0.01798	0.00026	0.44346	0.04846	0.00099	115.1	2.3	114.8	1.6	125	40	114.8	1.7	0.8431
PLC-51_2	152	55	29	0.1183	0.0026	0.01777	0.00027	0.42489	0.04824	0.00095	113.3	2.3	113.5	1.7	113	38	113.6	1.7	0.8430
PLC-51_3	94	27	15	0.1215	0.0041	0.01805	0.00029	0.37172	0.049	0.0016	116.4	3.5	115.3	1.8	154	53	115.2	1.8	0.8431
PLC-51_4	339	117	62	0.1166	0.002	0.01762	0.00025	0.60197	0.04784	0.00067	111.8	1.8	112.6	1.6	101	29	112.6	1.6	0.8430
PLC-51_5	109	37	20	0.1188	0.003	0.01796	0.00028	0.34173	0.048	0.0011	113.6	2.7	114.7	1.8	103	45	114.8	1.8	0.8430
PLC-51_6	120	41	22	0.1191	0.0031	0.01806	0.00027	0.26362	0.0478	0.0012	114.1	2.8	115.4	1.7	78	44	115.4	1.7	0.8431
PLC-51_7	342	133	73	0.1204	0.002	0.01808	0.00027	0.60527	0.0483	0.00064	115.5	1.8	115.5	1.7	119	27	115.5	1.7	0.8431
PLC-51_8	270	97	50	0.1187	0.0022	0.01775	0.00027	0.3842	0.04872	0.00084	113.5	2,0	113.4	1.7	131	33	113.4	1.7	0.8430
PLC-51_9	176	55	31	0.1208	0.0025	0.01803	0.00028	0.30798	0.0489	0.001	115.7	2.2	115.2	1.7	145	39	115.1	1.8	0.8431
PLC-51_10	127	45	24	0.1209	0.0031	0.01793	0.00027	0.34108	0.0488	0.0012	115.5	2.8	114.6	1.7	129	43	114.5	1.7	0.8430
PLC-51_11	156	66	35	0.1213	0.0025	0.01802	0.00026	0.48098	0.04906	0.0009	116.2	2.2	115.1	1.7	151	37	115.0	1.6	0.8431
PLC-51_12	138	44	25	0.1207	0.0061	0.018	0.00029	0.41306	0.0496	0.0021	115.3	5.3	115,0	1.8	148	66	114.8	1.9	0.8431
PLC-51_13	146	64	32	0.122	0.0028	0.01806	0.00029	0.37981	0.0492	0.0011	116.6	2.5	115.4	1.8	147	44	115.2	1.9	0.8431
PLC-51_14	123	36	19	0.1211	0.0032	0.01796	0.00029	0.41241	0.0495	0.0012	115.7	2.9	114.7	1.9	169	48	114.6	1.8	0.8430
PLC-51_15	209	74	40	0.1198	0.0024	0.01808	0.00028	0.43702	0.04842	0.00088	114.6	2.2	115.5	1.8	117	35	115.5	1.8	0.8431
PLC-51_16	126	49	27	0.122	0.0032	0.01807	0.00028	0.32869	0.0492	0.0012	116.5	2.8	115.4	1.8	153	46	115.3	1.8	0.8431
PLC-51_17	213	72	37	0.1189	0.0026	0.01804	0.00028	0.55981	0.04745	0.00087	113.9	2.4	115.2	1.8	86	36	115.4	1.8	0.8431
PLC-51_18	130	51	27	0.1204	0.0033	0.01799	0.00028	0.14168	0.0492	0.0012	115,0	3.0	115.1	1.8	135	44	114.8	1.8	0.8431
PLC-51_19	153	48	26	0.1197	0.0024	0.01794	0.00029	0.43309	0.04813	0.00097	114.6	2.2	114.6	1.9	118	39	114.6	1.8	0.8430
PLC-51_20	540	191	96	0.1172	0.0018	0.01731	0.00026	0.63488	0.04874	0.00057	112.4	1.6	110.6	1.7	133	25	110.5	1.6	0.8428
PLC-51_21	119	46	26	0.1256	0.003	0.01814	0.00027	0.36184	0.0501	0.0011	119.8	2.7	115.9	1.7	179	43	115.6	1.7	0.8431
PLC-51_22	258	67	36	0.121	0.0022	0.0179	0.00027	0.67281	0.04865	0.00074	115.8	2,0	114.4	1.7	131	30	114.3	1.7	0.8430
PLC-51_23	78	24	13	0.1221	0.0036	0.01786	0.00029	0.30782	0.0501	0.0015	117.2	3.3	114.1	1.8	176	56	113.9	1.8	0.8430
PLC-51_24	135	45	24	0.1195	0.0027	0.01797	0.00027	0.42839	0.0481	0.001	114.3	2.4	114.8	1.7	104	40	114.8	1.7	0.8431
PLC-51_25	110	37	21	0.1219	0.0032	0.01804	0.00028	0.34823	0.0494	0.0012	116.8	2.8	115.3	1.8	165	49	115.1	1.8	0.8431
PLC-51_26	114	41	23	0.1189	0.003	0.01784	0.00028	0.30982	0.0486	0.0012	113.7	2.7	114,0	1.8	128	46	113.9	1.8	0.8430
PLC-51_27	137	47	26	0.1198	0.0029	0.01796	0.00028	0.459	0.0487	0.001	114.9	2.6	114.7	1.8	138	42	114.7	1.8	0.8430
PLC-51_28	174	82	44	0.1189	0.0025	0.01791	0.00027	0.4993	0.04827	0.00094	113.8	2.2	114.4	1.7	114	38	114.4	1.7	0.8430
PLC-51_29	120	38	20	0.1207	0.0035	0.01787	0.00029	0.21913	0.0494	0.0013	115.2	3.2	114.3	1.8	145	46	114.0	1.8	0.8430
PLC-51_30	122	47	25	0.117	0.0028	0.01786	0.00028	0.29063	0.0474	0.0011	112.2	2.5	114.1	1.8	81	44	114.2	1.8	0.8430

Weighted Mean age (Ma±2σ): 114.7±0.3

MSWD: 0.70

table 1A continued.

				Isotopic Ratios						Age (Ma)							
análisis	**U**	**Th**	**Pb**	**$^{206}Pb/^{238}U$**	**error**	**$^{208}Pb/^{232}Th$**	**error**	**$^{207}Pb/^{206}Pb$**	**error**	**$^{206}Pb/^{238}U$**	**error**	**$^{208}Pb/^{232}Th$**	**error**	**$^{207}Pb/^{206}Pb$**	**error**	**$^{206}Pb/^{238}U(a)$**	**error**
	ppm	**ppm**	**ppm**	**ratio**	**1σ%**	**ratio**	**1σ%**	**ratio**	**1σ%**	**age**	**1σ%**	**age**	**1σ%**	**age**	**1σ%**	**age**	**1σ%**
UN-9675																	
AU20A126	499	478	12	0.0168	2,00%	0.0055	2.5%	0.0557	4.4%	107	2	110	3	439	49	106	2
AU20A133	183	109	4	0.0168	2.3%	0.0056	3.7%	0.049	6.4%	108	3	112	4	148	75	107	3
AU20A131	134	81	3	0.0171	2.7%	0.0055	3.7%	0.0493	7.7%	109	3	112	4	160	89	109	3
AU20A123	162	100	4	0.0174	2.6%	0.0054	4.3%	0.0521	7.7%	111	3	109	5	289	88	110	3
AU20A134	91	46	2	0.0175	3.4%	0.0063	5.3%	0.0529	8.4%	112	4	128	7	326	96	111	4
AU20A128	117	45	2	0.0177	3,00%	0.0058	5.8%	0.055	7.5%	113	3	117	7	411	84	112	3
AU20A120	114	45	2	0.0177	2.8%	0.006	5.7%	0.0532	7.8%	113	3	121	7	337	89	113	3
AU20A127	138	63	3	0.0177	2.7%	0.0056	4.5%	0.0526	7.5%	113	3	113	5	313	85	113	3
AU20A121	171	85	4	0.0177	2.4%	0.0058	4.1%	0.0416	7.5%	113	3	116	5	-251	95	113	3
AU20A124	183	103	4	0.0177	2.3%	0.0067	3.4%	0.0481	7.00%	113	3	135	5	102	83	113	3
AU20A122	141	98	3	0.0181	3.0%	0.0055	4.6%	0.0505	6.9%	116	3	110	5	217	80	115	3
AU20A125	234	157	5	0.0184	2.5%	0.0057	4,00%	0.057	6.4%	117	3	114	5	490	71	116	3
AU20A130	169	96	4	0.0183	2.5%	0.0055	4,00%	0.0445	6.3%	117	3	112	4	-82	77	117	3
AU20A129	151	100	4	0.0183	2.5%	0.0056	3.6%	0.0452	7.00%	117	3	114	4	-44	86	117	3
AU20A132	100	57	2	0.019	2.8%	0.0062	4.9%	0.0549	8.2%	121	3	124	6	409	92	120	3

Weighted Mean Age (Ma±2σ): 112.0±2.1

MSWD: 1.7

				Isotopic Ratios						Age (Ma)							
sample	**U**	**Th**	**Pb**	**$^{206}Pb/^{238}U$**	**error**	**$^{208}Pb/^{232}Th$**	**error**	**$^{207}Pb/^{206}Pb$**	**error**	**$^{206}Pb/^{238}U$**	**error**	**$^{208}Pb/^{232}Th$**	**error**	**$^{207}Pb/^{206}Pb$**	**error**	**$^{206}Pb/^{238}U(a)$**	**error**
	ppm	**ppm**	**ppm**	**ratio**	**1σ%**	**ratio**	**1σ%**	**ratio**	**1σ%**	**age**	**1σ%**	**age**	**1σ%**	**age**	**1σ%**	**age**	**1σ%**
PY-01																	
AU20A039	153	105	3	0.0145	3.5%	0.0081	5.4%	0.1158	7.9%	93	3	163	9	1,893	71	85	3
AU20A038	211	140	4	0.0134	2.7%	0.0045	3.8%	0.0555	7.2%	86	2	91	3	433	80	85	2
AU20A036	244	143	4	0.0134	2.6%	0.0043	4,00%	0.0407	7.7%	86	2	86	3	-306	98	86	2
AU20A033	178	166	3	0.0135	3,00%	0.004	3.8%	0.0497	8.2%	86	3	81	3	183	95	86	3
AU20A027	267	136	4	0.0136	2.5%	0.0046	4.4%	0.0472	7.3%	87	2	92	4	61	87	87	2
AU20A034	203	134	4	0.0137	2.6%	0.0042	4,00%	0.0531	6.6%	88	2	85	3	334	75	87	2
AU20A035	275	220	5	0.0138	2.2%	0.0046	3,00%	0.0584	6.4%	88	2	93	3	546	70	87	2
AU20A037	199	128	4	0.0138	2.5%	0.0048	3.8%	0.0563	6.7%	88	2	96	4	463	74	87	2
AU20A028	198	140	4	0.0137	2.8%	0.0044	4.2%	0.0446	6.9%	88	2	88	4	-77	85	88	2
AU20A032	262	179	5	0.014	2.4%	0.0054	3.1%	0.0611	5.5%	90	2	109	3	644	59	88	2
AU20A040	147	71	3	0.0138	3.6%	0.0043	6.3%	0.0501	10.7%	88	3	86	5	201	124	88	3
AU20A031	221	153	4	0.0138	2.6%	0.0046	3.7%	0.0433	6.7%	88	2	93	3	-149	83	88	2
AU20A029	259	190	5	0.0146	2.3%	0.0062	3.1%	0.0805	5,00%	93	2	125	4	1,210	49	90	2
AU20A026	141	79	2	0.0142	2.9%	0.0043	5.1%	0.0528	9.3%	91	3	86	4	319	105	90	3
AU20A030	150	80	3	0.0142	3.7%	0.0045	5.7%	0.054	8.7%	91	3	91	5	371	98	90	3

Weighted Mean age (Ma±2σ): 87.4±1.2

MSWD: 0.40

table 1A continued.

				Isotopic Ratios						Age (Ma)						
sample	U	Th	Pb	$^{206}Pb/^{238}U$	error	$^{208}Pb/^{232}Th$	error	$^{207}Pb/^{206}Pb$	error	$^{206}Pb/^{238}U$	error	$^{208}Pb/^{232}Th$	error	$^{207}Pb/^{206}Pb$	error	$^{206}Pb/^{238}U(a)$	error
	ppm	ppm	ppm	ratio	1σ%	ratio	1σ%	ratio	1σ%	age	1σ%	age	1σ%	age	1σ%	age	1σ%
SVD-08																	
MA25A236	162	100	3	0.0137	1.4%	0.0041	3.6%	0.0528	4.3%	88	1	82	3	319	97	87	1
MA25A231	130	89	2	0.0136	1.7%	0.0047	5.5%	0.0493	5.7%	87	2	96	5	162	133	87	2
MA25A237	182	87	3	0.014	1.4%	0.0046	4.1%	0.0472	4.5%	89	1	93	4	58	107	90	1
MA25A235	229	134	4	0.0141	1.4%	0.0044	4.7%	0.0488	4,00%	90	1	89	4	138	94	90	1
MA25A250	264	164	4	0.0141	1.4%	0.0047	8.5%	0.0481	3.9%	90	1	94	8	106	92	90	1
MA25A233	399	266	7	0.014	1.1%	0.0047	2.1%	0.0473	2.4%	90	1	94	2	63	57	90	1
MA25A232	115	75	2	0.0141	1.6%	0.0045	4.5%	0.0471	5.7%	90	1	91	4	54	135	90	1
MA25A247	109	72	2	0.014	1.9%	0.0041	6.9%	0.0427	6.1%	90	2	83	6	-187	152	90	2
MA25A234	239	187	4	0.0141	1.5%	0.0047	8.4%	0.0483	4.3%	91	1	95	8	114	101	90	1
MA25A246	154	75	2	0.0142	1.7%	0.0042	4.9%	0.0469	5.3%	91	2	85	4	46	126	91	2
MA25A230	113	73	2	0.0141	1.8%	0.0046	4.8%	0.0444	5.3%	91	2	93	4	-90	130	91	2
MA25A249	155	79	3	0.0142	1.6%	0.0044	5.5%	0.0452	4.6%	91	1	89	5	-43	112	91	1
MA25A240	186	98	3	0.0144	2,00%	0.0047	6.3%	0.0457	6.8%	92	2	95	6	-16	164	93	2
MA25A248	196	134	4	0.0147	1.6%	0.0053	6.1%	0.0589	5.4%	94	1	107	7	563	118	93	1
MA25A245	87	39	2	0.0145	2.2%	0.0051	7.3%	0.0439	7.1%	93	2	103	7	-115	175	93	2

Weighted Mean Age (Ma±2σ): 90.13±0.91

MSWD: 1.4

				Isotopic Ratios						Age (Ma)						
sample	U	Th	Pb	$^{206}Pb/^{238}U$	error	$^{208}Pb/^{232}Th$	error	$^{207}Pb/^{206}Pb$	error	$^{206}Pb/^{238}U$	error	$^{208}Pb/^{232}Th$	error	$^{207}Pb/^{206}Pb$	error	$^{206}Pb/^{238}U(a)$	error
	ppm	ppm	ppm	ratio	1σ%	ratio	1σ%	ratio	1σ%	age	1σ%	age	1σ%	age	1σ%	age	1σ%
EL-9674																	
AU20A112	777	627	14	0.0141	1.8%	0.0043	2.5%	0.0524	4,00%	90	2	87	2	303	46	90	2
AU20A104	84	42	2	0.0145	4,00%	0.0048	6.1%	0.067	10.9%	93	4	96	6	837	114	91	4
AU20A110	406	276	7	0.0144	3.5%	0.0046	3.9%	0.0524	9,00%	92	3	92	4	301	103	91	3
AU20A106	2,841	2,708	60	0.0143	1.4%	0.0048	1.8%	0.0487	2,00%	92	1	97	2	133	24	92	1
AU20A101	389	256	7	0.0143	2.1%	0.0047	3.3%	0.0484	5.6%	92	2	94	3	121	66	92	2
AU20A111	347	240	6	0.0144	2.3%	0.0047	3.2%	0.0501	6.2%	92	2	95	3	202	72	92	2
AU20A102	600	423	11	0.0146	1.9%	0.0051	2.5%	0.0594	4,00%	93	2	103	3	583	44	92	2
AU20A103	334	151	6	0.0145	2.6%	0.0051	4.2%	0.0541	6.1%	93	2	103	4	373	69	92	2
AU20A107	331	229	7	0.0145	2.3%	0.0047	3.4%	0.0512	6.8%	93	2	95	3	248	78	92	2
AU20A105	570	378	10	0.0145	2.3%	0.0048	3.3%	0.0495	6.1%	93	2	96	3	174	71	92	2
AU20A114	247	137	4	0.0145	2.4%	0.0046	3.5%	0.049	5.9%	93	2	93	3	150	69	93	2
AU20A109	596	400	10	0.0146	3.3%	0.0045	4.5%	0.0471	6.6%	94	3	91	4	52	79	94	3
AU20A100	298	152	6	0.0152	2.2%	0.0055	4.3%	0.0528	5.8%	97	2	112	5	321	66	97	2
AU20A113	294	178	6	0.0153	2.3%	0.0051	3.1%	0.0522	5.6%	98	2	103	3	295	64	97	2
AU20A108	234	118	5	0.0165	2.2%	0.0056	3.5%	0.0517	5.9%	105	2	114	4	274	67	105	2

Weighted Mean Age (Ma±2σ): 92.4±1.1

MSWD: 0.9

Analytical Procedures Table 1A

LA-ICPMS zircon geochronology at the University of Tasmania

The LA-ICPMS method is now widely used for measuring U, Th and Pb isotopic data.

Approximately 100 g of rock was crushed in a Cr-steel ring mill to a grain size <400 micron. Non magnetic heavy minerals were then separated using a gold pan and a Fe-B-Nd hand magnet for the magnetic fraction. The zircons were hand picked from the heavy mineral concentrate under the microscope in cross-polarised transmitted light. The selected crystals were placed on double sided sticky tape and epoxy glue was then poured into a 2.5 cm diameter mould on top of the zircons. The mount was dried for 12 hours and polished using clean sandpaper and a clean polishing lap. The samples were then washed in distilled water in an ultrasonic bath.

The analyses in this study were performed on an Agilent 7500cs quadrupole ICPMS with a 193 nm Coherent Ar-F gas laser and the Resonetics S155 ablation cell at the University of Tasmania in Hobart. The downhole fractionation, instrument drift and mass bias correction factors for Pb/U ratios on zircons were calculated using 2 analyses on the primary (91500 standard of Wiendenbeck *et al.* (1995)) and checked on 1 analysis on each of the secondary standard zircons (Temora standard of Black *et al.* (2003) and JG1 of Jackson *et al*. (2004)) analysed at the beginning of the session and every 15 unknown zircons (roughly every 1/2 hour) using the same spot size and conditions as used on the samples. Additional secondary standards (The Mud Tank Zircon of Black and Gulson (1978), Penglai zircons of Li *et al*. (2010), and the Plesovice zircon of Slama *et al*. (2008)) were also analysed. The correction factor for the $^{207}Pb/^{206}Pb$ ratio was calculated using large spots of NIST610 analysed every 30 unknowns and corrected using the values recommended by Baker *et al*. (2004).

Each analysis on the zircons began with a 30 second blank gas measurement followed by a further 30 seconds of analysis time when the laser was switched on. Zircons were sampled on 32 micron spots using the laser at 5 Hz and a density of approximately 2 J/cm^2. A flow of He carrier gas at a rate of 0,35 litres/minute carried particles ablated by the laser out of the chamber to be mixed with Ar gas and carried to the plasma torch. Isotopes measured were ^{49}Ti, ^{56}Fe, ^{90}Zr, ^{178}Hf, ^{202}Hg, ^{204}Pb, ^{206}Pb, ^{207}Pb, ^{208}Pb, ^{232}Th and ^{238}U with each element being measured every 0.16 s with longer counting time on the Pb isotopes compared to the other elements. The data reduction used was based on the method outlined in detail in Meffre *et al*. (2008) and Sack *et al*. (2011) similar to that outlined in Black *et al*. (2004) and Paton *et al*. (2010). Uncertainties were calculated using methods similar to that outlined Paton *et al.* (2010).

Element abundances on zircons were calculated using the method outlined by Kosler (2001) using Zr as the internal standard element, assuming stoichiometric proportions and using the NIST610 to standard correct for mass bias and drift.

References

Baker, J.; Peate, D.; Waight, T.; Meyzen, C. 2004. Pb isotopic analysis of standards and samples using a 207Pb-204Pb double spike and Thallium to correct for mass bias with a double focusing MC-ICP-MS. Chemical Geology 211 (3-4): 275-303. doi: 10.1016/j.chemgeo.2004.06.030.

Black, L.P.; Gulson, B.L. 1978. The age of the Mud Tank Carbonatite, Strangways Range, Northern Territory. Bureau of Mineral Resources, Journal of Australian Geology and Geophysics 3: 227-232.

Black, L.P.; Kamos, L.; Allen, C.M.; Aleinikoff, J.N.; Davis, D.W.; Korsch, R.J.; Foudoulis, C. 2003. TEMORA 1: a new zircon standard for Phanerozoic U-Pb geochronology. Chemical Geology 200: 155-170.

Black, L.P.; Kamo, S.L.; Allen, C.M.; Davis, D.W.; Aleninikoff, J.N.; Valley, J.W.; Mundil, R.; Campbell, I.H.; Korsch, R.J.; Williams, I.S.; Foudoulis, C. 2004. Improved $^{206}Pb/^{238}U$ microprobe geochronology by the monitoring of a trace-element related matrix effect; SHRIMP, ID-TIMS, ELA-ICP-MS, and oxygen isotope documentation for a series of zircon standards. Chemical Geology 205: 115-140.

Jackson, S.E.; Pearson, N.J.; Griffin, W.L.; Belousova, E.A. 2004. The application of laser ablation-inductively coupled plasma-mass spectrometry to in situ U-Pb zircon geochronology. Chemical Geology 211: 47-69.

Kosler J (2001) Laser-ablation ICPMS study of metamorphic minerals and processes. *In* Laser-ablation-ICPMS in the earth sciences; principles and applications (Sylvester, P.J.; editor). Mineralogical Association of Canada Short Course Handbook 29: 185-202.

Meffre, S.; Large, R.R.; Scott, R.; Woodhead, J.; Chang, Z.; Gilbert, S.E.; Danyushevsky, L.V.; Maslennikov, V.; Hergt, J.M. 2008. Age and pyrite Pb-isotopic composition of the giant Sukhoi Log sediment-hosted gold deposit, Russia. Geochimica et Cosmochimica Acta 72: 2377-2391.

Li, X.; Long, W.G.; Li, Q.L.; Liu, Y.; Zheng, Y.F.; Yang, Y.H.; Chamberlain, K.R.; Wan, D.F.; Guo, C.H.; Wang, X.C.; Tao, H. 2010. Penglai zircon megacrysts: A potential new working reference material for microbeam determination of Hf-O isotopes and U-Pb age. Geostandards and Geoanalytical Research 34: 117-134.

Paton, C.; Woodhead, J.D.; Hellstrom, J.C.; Hergt, J.M.; Greig, A.; Maas, R. 2010. Improved laser ablation U-Pb zircon geochronology through robust down-hole fractionation correction. Geochemistry, Geophysics, Geosystems11: 1525-2027

Sack, P.J.; Berry, R.F.; Meffre, S.; Falloon, T.J.; Gemmell, J.B.; Friedman, R.M. 2011. In situ location and U-Pb dating of small zircon grains in igneous rocks using laser ablation-inductively coupled plasma-quadrupole mass spectrometry. Geochemistry, Geophysics, Geosystems 12: 23 p. doi:10.1029/2010GC003405.

Slama, J.; Kosler, J.; Condon, D.J.; Crowley, J.L.; Gerdes, A.; Hanchar, J.M.; Horstwood, M.S.A.; Morris, G.A.; Nasdala, L.; Norberg, N.; Schaltegger, U.; Schoene, B.; Tubrett, M.N.; Whitehouse, M.J. 2008. Plesovice zircon-A new natural reference material for U-Pb and Hf isotopic microanalysis. Chemical Geology 249: 1-35.

LA-ICPMS zircon geochronology at Sernageomin

Samples were previously crushed under 500 µm and heavy minerals were concentrated using a Gemini water table. The resulting sample was examined under a UV lamp in a microscope and zircon crystals were selected by hand picking. A number between 30 and 120 zircon crystals were mounted in a 2.5 cm diameter epoxy briquette, together with a Temora 2 (Black *et al*., 2004) crystal. After mounting, cathodoluminiscence and backscattered electron images were obtained under electronic microscope (Zeiss MA-10), to obtain an detailed image of zoning patterns, inherited cores, inclusions and fractures in zircon crystals.

Samples for U-Pb dating were analyzed by laser ablation in a Photon-Machines equipment, Analyte 193.G2 eximer model. Several briquette samples are mounted together with a briquette with GJ-1 primary standar (Jackson *et al*., 2004) and Mud Tank (Black and Gulson, 1978) and Plesovice (Sláma *et al*., 2008) as secondary standars. The ablation diameter in the zircon crystals was 30 µm, with a pulse frequency of 9 Hz and energy density about 2 mJ/cm, producing a crater of 15-20 µm depth in the zircon crystals.

After ablation, isotopes and elements concentration (U, Pb and Th) were measured in a Thermo Fischer Element XR double focus mass spectrometer, with an electron multiplier. Data reduction done using Iolite software (Petrus and Kamber, 2012). Isotope fractionation produced during ablation and along the spectrometer, instrumental drift and calibration of isotope ratios, were controlled through analyses on the primary standar GJ-1. Second order variations related to sample position on the ablation chamber on the Photon-Machines equipment, were corrected by measurements on the Temora 2 estándar mounted in every simple briquette. Secondary standards (Plesovice and Mud Tank) are considered as unknown samples and therefore as quality control on the analyses. For Phanerozoic samples, $^{206}Pb/^{238}U$ ages are corrected for common-Pb using the 207-method of Williams (1998). Final results, age calculations and graphics have been extracted using the Isoplot tool for Microsoft Excel (Ludwig, 2012). The decay constants are those defined by Steiger and Jäger (1977).

TABLE 2A. MAJOR AND TRACE ELEMENTS CONTENTS IN ROCK SAMPLES OF PUNTA DEL COBRE, BANDURRIAS, CERRILLOS AND VIÑITA FORMATIONS AND DACITE PORPHYRIES.

Sample	ACh -5q	ACh -7q	ACh -12q	ACh -25q	ACH - 220q	ACH - 221q	CCH - 132q	ACH-142q	CCH - 133q	CCH - 134q	MCh - 83q	ACh - 81q
Formation	Punta del Cobre	Punta del Cobre	Punta del Cobre	Punta del Cobre	Punta del Cobre	Punta del Cobre	Punta del Cobre	Punta del Cobre	Punta del Cobre	Punta del Cobre	Punta del Cobre	Punta del Cobre
Age (Ma)	140	140	143	135	135	135	133	134	128	127	133	125
Lithology	andesitic lava	andesitic lava	andesitic lava	andesitic lava	andesitic lava	andesitic lava	andesite hornfels	riolite dome	andesite lava	brecciated lava	andesitic dike	dacite lava
wt.%												
SiO_2	53.28	52.86	56.51	49.14	51.17	51.59	53.77	77.20	51.87	54.72	56.69	60.22
Al_2O_3	17.09	15.33	15.76	18.69	15.20	16.29	15.78	11.55	18.06	18.10	15.76	16.24
TiO_2	1.04	1.09	1.25	1.87	2.17	1.26	1.14	1.12	1.23	0.73	1.10	0.75
Fe_2O_3	11.11	7.71	8.86	6.76	11.47	15.28	10.65	1.30	9.87	7.53	4.59	7.78
CaO	3.02	6.22	6.99	15.02	4.38	2.49	7.01	0.29	9.92	2.08	11.26	2.59
MgO	5.08	3.10	3.54	0.52	5.49	1.78	4.99	0.69	3.87	3.07	4.88	3.05
MnO	0.12	0.26	0.17	0.18	0.15	0.07	0.04	0.17	0.13	0.26	0.13	0.09
Na_2O	5.62	5.64	3.06	4.07	3.88	5.87	3.74	0.28	3.28	5.08	3.91	6.42
K_2O	0.45	0.96	2.48	2.91	1.10	2.79	1.78	4.08	0.88	4.31	0.46	0.78
P_2O_5	0.16	0.20	0.23	0.21	0.28	0.19	0.13	0.19	0.14	0.08	0.02	0.15
LOI	2.86	6.29	0.88	0.44	4.45	2.18	0.75	2.81	0.59	3.55	0.74	1.69
SUMA	99.82	99.67	99.74	99.81	99.73	99.79	99.78	99.67	99.85	99.51	99.54	99.76
ppm												
Cu	4.00	31.00	73.00	14.00	46.00	13.00	18.00	7.00	43.00	24.00	11.00	73.00
Pb	b.d.l.	b.d.l.	b.d.l.	b.d.l.	b.d.l.	b.d.l.	b.d.l.	b.d.l.	b.d.l.	b.d.l.	b.d.l.	b.d.l.
Ni	13.00	63.00	11.00	b.d.l.	23.00	14.00	26.00	b.d.l.	20.00	b.d.l.	5.00	b.d.l.
Co	15.00	8.00	16.00	6.00	28.00	8.00	18.00	b.d.l.	23.00	16.00	8.00	10.00
Zn	28.00	20.00	73.00	16.00	30.00	20.00	21.00	7.00	44.00	157.00	37.00	42.00
Cr	72.00	135.00	46.00	22.00	52.50	36.03	68.05	26.34	64.61	1.63	48.73	12.37
Sc	26.00	22.00	25.00	28.00	-	-	-	-	-	-	-	-
V	230.00	202.00	209.00	339.00	387.50	113.70	274.70	143.50	287.80	196.80	148.40	176.70
Nb	6.70	7.38	8.22	4.74	8.61	2.69	3.56	4.43	3.32	2.56	3.75	5.89
Zr	220.00	238.00	276.00	204.00	197.20	90.88	131.40	150.20	98.20	51.65	124.00	133.50
U	2.03	2.51	2.71	0.93	1.67	1.22	1.44	-	0.65	0.43	0.76	1.25
Th	9.21	11.53	10.36	3.04	5.39	4.43	2.97	-	2.01	1.60	0.41	4.79
Rb	7.00	26.00	84.00	63.00	37.00	49.00	69.00	96.00	19.00	101.00	12.00	25.00
Sr	193.00	115.00	358.00	317.00	165.40	89.36	300.50	15.45	284.20	183.20	342.40	282.20
Ba	75.00	71.00	387.00	227.00	105.60	235.30	178.30	143.50	194.80	993.80	102.20	185.50
Y	25.71	24.24	34.37	35.88	44.67	25.15	22.07	30.53	26.53	13.16	31.41	23.29
Cs	0.22	0.77	1.53	0.81	1.87	0.16	1.65	-	0.23	1.63	0.36	<0.10
Hf	4.02	5.56	6.42	3.82	6.40	2.75	4.19	-	3.36	1.83	2.92	3.28
Ta	-	-	-	-	0.82	0.21	0.28	-	0.25	0.26	0.14	0.35
La	23.56	32.60	30.89	19.26	25.75	16.88	18.84	5.19	14.20	7.67	5.64	11.35
Ce	50.33	72.01	68.76	43.80	61.17	37.62	41.81	12.04	33.84	16.62	15.69	25.58
Pr	6.42	8.67	8.51	5.73	7.72	4.64	4.88	1.62	4.43	2.11	2.45	3.25
Nd	28.66	38.50	38.60	27.10	37.28	20.52	21.80	5.73	21.03	10.18	13.94	14.85
Sm	5.63	6.71	7.58	6.05	8.82	4.48	4.90	1.71	5.02	2.35	3.93	3.10
Eu	1.24	1.46	1.57	1.70	1.93	1.36	1.53	0.45	1.45	0.76	0.85	0.92
Gd	4.89	5.31	6.53	6.09	8.69	4.41	4.67	3.36	5.10	2.33	4.33	3.14
Tb	0.75	0.73	0.98	0.99	1.36	0.74	0.71	0.71	0.81	0.38	0.79	0.55
Dy	4.42	4.17	5.83	6.12	8.53	4.79	4.39	5.01	5.29	2.50	5.13	3.52
Ho	0.90	0.85	1.22	1.28	1.77	1.01	0.91	1.13	1.10	0.53	1.11	0.81
Er	2.33	2.31	3.30	3.43	4.86	2.72	2.51	3.32	3.11	1.51	3.20	2.37
Tm	0.33	0.34	0.47	0.48	0.70	0.38	0.35	0.49	0.44	0.22	0.47	0.36
Yb	2.06	2.29	3.04	3.02	4.40	2.44	2.41	3.10	2.97	1.52	3.03	2.39
Lu	0.30	0.34	0.45	0.43	0.63	0.36	0.35	0.45	0.42	0.22	0.46	0.36

table 2A. continued.

Sample	ACh - 84q	ACh - 104q	ACh - 106q	ACH - 217q	ACH - 218q	ACH - 219q	CCH - 123q	CCh - 51Bq	ACh - 107q	ACh - 110q	ACH-140q	ACH - 216q
Formation	Punta del Cobre	Punta del Cobre	Punta del Cobre	Punta del Cobre	Punta del Cobre	Punta del Cobre	Punta del Cobre	Bandurrias	Bandurrias	Cerrillos	Bandurrias	Bandurrias
Age	125	117	112	124	118	128	118	116	114	94	114	112
Lithology	dacite dome	andesite dome	volcanic breccia	andesite lava	basalt lava	andesite lava	andesite lava	tuff	andesite	andesite	andesite	basalt
wt.%												
SiO_2	62.98	50.76	55.07	61.48	49.29	52.03	53.97	73.76	53.72	52.44	53.51	50.54
Al_2O_3	16.37	17.78	16.84	16.08	16.48	19.40	15.27	11.03	15.92	16.83	16.39	17.06
TiO_2	0.58	0.91	0.97	0.77	0.78	0.84	0.65	0.48	0.89	1.04	0.87	0.92
Fe_2O_3	5.53	8.87	8.75	6.42	11.99	8.85	8.23	4.62	9.41	9.21	8.74	9.03
CaO	1.49	5.34	5.62	2.85	3.64	9.48	4.32	0.29	8.39	8.33	5.44	6.61
MgO	2.81	5.52	3.59	2.19	2.69	3.73	2.00	0.14	4.59	4.82	4.32	4.43
MnO	0.01	0.46	0.18	0.07	0.27	0.05	0.21	0.04	0.16	0.14	0.32	0.15
Na_2O	8.76	3.38	2.72	8.63	1.98	2.96	2.81	0.01	2.74	2.65	2.36	3.48
K_2O	0.11	2.19	3.38	0.63	7.99	1.30	7.85	8.13	1.69	2.21	4.21	2.09
P_2O_5	0.14	0.26	0.28	0.06	0.07	0.07	0.05	0.07	0.22	0.23	0.10	0.11
LOI	0.77	4.33	2.22	0.63	4.70	1.05	4.47	1.00	0.87	1.65	3.36	5.09
SUMA	99.55	99.80	99.61	99.81	99.87	99.77	99.84	99.56	98.59	99.55	99.62	99.52
ppm												
Cu	71.00	10.00	11.00	8.00	9.00	12.00	34.00	24.00	335.00	134.00	60.00	19.00
Pb	b.d.l.	11.00	8.00	4.00	10.00	b.d.l.	b.d.l.	18.00	5.00	6.00	14.00	5.00
Ni	b.d.l.	b.d.l.	b.d.l.	b.d.l.	b.d.l.	2.00	b.d.l.	b.d.l.	5.00	9.00	b.d.l.	b.d.l.
Co	b.d.l.	35.00	21.00	3.00	37.00	15.00	20.00	b.d.l.	23.00	23.00	24.00	23.00
Zn	11.00	477.00	76.00	22.00	208.00	19.00	160.00	55.00	84.00	87.00	144.00	186.00
Cr	8.92	10.01	7.45	9.06	9.24	16.86	11.97	15.52	44.44	36.39	27.72	10.37
Sc	-	-	-	-	-	-	-	-	-	-	-	-
V	119.50	263.50	249.70	168.90	234.50	265.50	157.50	88.77	287.70	268.30	1144.00	278.20
Nb	b.d.l.	b.d.l.	4.93	1.60	1.44	1.60	1.51	b.d.l.	3.75	3.96	4.49	3.33
Zr	99.68	78.75	113.90	98.82	68.81	51.35	77.96	58.87	104.60	154.60	117.30	85.85
U	-	-	2.41	0.68	0.77	0.24	0.77	-	1.89	1.52	3.59	1.38
Th	-	-	8.89	2.96	2.82	0.81	3.28	-	7.60	5.88	14.13	4.89
Rb	4.00	90.00	80.00	12.00	212.00	41.00	162.00	192.00	53.00	68.00	118.00	94.00
Sr	68.69	548.10	598.40	72.56	65.76	308.80	53.94	24.09	469.70	455.20	435.50	661.90
Ba	4.89	484.20	841.00	22.43	1991.00	111.30	909.20	1052.00	460.60	326.70	1144.00	373.20
Y	16.61	20.90	26.45	16.82	20.85	15.99	13.84	9.10	25.40	31.55	23.39	20.38
Cs	-	-	2.34	b.d.l.	1.92	1.34	0.86	-	1.11	2.10	2.45	3.62
Hf	-	-	3.16	3.21	2.31	1.65	2.71	-	2.86	4.15	2.92	2.73
Ta	-	-	0.54	0.14	b.d.l.	b.d.l.	0.14	-	0.45	0.47	0.28	0.28
La	5.97	22.34	23.73	4.42	7.51	6.43	6.28	7.38	25.30	24.48	18.23	14.30
Ce	15.09	46.02	49.96	13.18	18.00	14.70	14.48	14.20	44.66	49.62	40.66	30.11
Pr	2.22	5.50	6.20	1.96	2.41	1.95	1.95	1.81	5.34	6.27	5.13	3.72
Nd	11.21	24.91	28.20	9.61	11.66	9.45	9.30	7.88	23.42	29.12	22.00	16.78
Sm	2.42	4.60	5.27	2.41	3.02	2.46	2.27	1.43	4.57	6.12	4.83	3.84
Eu	0.71	1.27	1.31	0.88	0.79	0.93	0.51	0.42	1.14	1.49	1.18	1.15
Gd	2.29	3.95	4.63	2.48	3.20	2.59	2.25	1.35	3.98	5.41	4.57	3.59
Tb	0.39	0.57	0.70	0.42	0.55	0.43	0.37	0.21	0.62	0.82	0.68	0.56
Dy	2.52	3.41	4.23	2.78	3.60	2.85	2.41	1.35	3.83	4.96	4.07	3.56
Ho	0.57	0.71	0.89	0.63	0.78	0.60	0.52	0.30	0.83	1.04	0.87	0.75
Er	1.69	1.93	2.51	1.83	2.22	1.70	1.50	0.93	2.31	2.81	2.51	2.11
Tm	0.26	0.28	0.36	0.28	0.33	0.24	0.22	0.14	0.33	0.40	0.37	0.32
Yb	1.77	1.79	2.42	1.93	2.23	1.65	1.58	1.06	2.20	2.64	2.39	2.11
Lu	0.27	0.26	0.37	0.31	0.33	0.24	0.24	0.16	0.33	0.40	0.37	0.32

table 2A. continued.

Sample	ACH - 215q	ACh - 113q	CCH-73q	CCH-75q	ACH-135q	ACH-136q	ACH-147q	ACH-148q	ACH-149q	ACH-151q	ACH - 210q	ACH - 211q
Formation	Bandurrias	Fm Cerrillos (toba)	Fm Cerrillos lava 2	Fm Cerrillos lava 2	Fm Cerrillos lava 2	Fm Cerrillos lava 2	Fm Cerrillos lava 2	Fm Cerrillos lava 2	Fm Cerrillos lava 2	Fm Cerrillos lava 2	Fm Cerrillos lava 2	Fm Cerrillos lava 2
Age	112	92	94	92	93	92	105	94	93	91	92	92
Lithology	basalt	welded tuff	andesite lava	andesite lava	andesite lava	andesite lava	andesite lava	andesite lava	andesite lava	andesite lava	andesite lava	andesite lava
wt.%												
SiO_2	48.81	64.17	44.56	57.94	61.99	54.65	55.02	61.09	52.35	53.67	52.52	49.34
Al_2O_3	16.99	15.17	14.47	17.09	16.81	18.53	18.62	16.52	17.83	17.89	17.04	17.23
TiO_2	0.96	0.95	1.57	0.89	0.66	1.09	1.15	0.82	1.01	1.19	1.40	1.68
Fe_2O_3	8.48	5.04	10.87	7.01	5.21	8.39	8.58	7.37	9.17	9.23	10.07	10.93
CaO	10.24	1.50	10.23	5.49	3.01	6.42	6.59	4.30	8.28	7.66	8.68	8.55
MgO	3.41	1.23	8.83	2.53	1.47	3.30	2.50	1.94	4.58	3.52	4.76	4.60
MnO	0.40	0.13	0.17	0.11	0.11	0.09	0.09	0.11	0.10	0.12	0.22	0.19
Na_2O	2.57	3.67	2.78	3.69	4.01	3.43	3.76	3.74	2.71	2.82	2.64	2.77
K_2O	2.01	6.13	1.36	2.82	4.70	2.06	2.05	2.98	2.19	2.19	1.62	1.76
P_2O_5	0.20	0.30	0.34	0.14	0.10	0.06	0.10	0.16	0.07	0.14	0.21	0.37
LOI	6.02	1.27	4.54	1.93	1.49	1.69	1.17	0.73	1.27	1.27	0.50	2.28
SUMA	100.08	99.56	99.72	99.64	99.57	99.70	99.64	99.76	99.56	99.70	99.66	99.70
ppm												
Cu	130.00	34.00	39.00	30.00	22.00	154.00	26.00	20.00	127.00	304.00	225.00	33.00
Pb	11.00	20.00	5.00	5.00	7.00	b.d.l.	4.00	b.d.l.	23.00	10.00	9.00	b.d.l.
Ni	3.00	b.d.l.	131.00	4.00	b.d.l.	b.d.l.	b.d.l.	b.d.l.	10.00	9.00	10.00	12.00
Co	32.00	7.00	40.00	16.00	9.00	19.00	15.00	12.00	27.00	43.00	25.00	24.00
Zn	96.00	239.00	99.00	108.00	66.00	78.00	73.00	69.00	98.00	197.00	107.00	179.00
Cr	22.58	b.d.l.	410.00	27.00	14.00	15.48	225.50	139.40	56.55	14.61	33.42	41.64
Sc	-	-	-	-	-	-	-	-	-	-	-	-
V	278.40	76.00	298.00	180.00	729.00	459.80	480.20	488.30	272.20	337.40	261.60	272.70
Nb	5.90	10.00	13.51	9.54	10.10	5.10	5.98	6.75	4.18	5.11	6.59	11.73
Zr	120.10	197.00	138.00	202.00	277.60	149.20	149.80	243.70	153.30	208.70	198.20	347.10
U	3.31	5.79	1.23	2.76	4.80	1.07	1.46	2.13	1.82	2.02	1.44	2.29
Th	11.71	14.25	4.87	9.65	19.06	4.42	5.45	9.04	7.12	8.87	5.20	8.08
Rb	37.00	162.00	32.00	84.00	137.00	43.00	37.00	88.00	56.00	49.00	30.00	43.00
Sr	666.50	104.00	663.00	438.00	571.80	491.00	497.20	329.00	447.50	505.20	483.10	533.50
Ba	998.90	1009.00	776.00	457.00	729.00	459.80	480.20	488.30	272.20	337.40	291.20	415.20
Y	20.81	49.43	24.69	27.02	31.03	27.40	25.68	36.51	26.31	37.23	31.93	44.89
Cs	2.09	2.44	126.50	2.12	2.95	1.22	1.86	2.94	0.74	1.17	1.63	1.64
Hf	3.75	8.22	3.53	4.89	7.12	3.59	3.33	5.81	3.22	5.55	5.89	9.32
Ta	0.67	0.63	0.94	0.86	0.88	0.28	0.31	0.38	0.19	0.51	0.52	1.02
La	27.15	40.97	38.49	21.82	28.91	18.30	17.66	23.94	16.76	25.39	22.13	34.86
Ce	59.40	89.96	86.80	49.56	62.05	42.55	41.19	55.79	39.89	56.45	54.55	94.99
Pr	6.91	11.57	11.44	6.38	7.64	5.52	5.37	7.19	5.23	7.46	6.93	11.58
Nd	30.35	50.16	50.59	27.06	31.10	24.78	23.70	33.06	23.73	33.91	33.42	53.79
Sm	6.10	9.67	10.75	5.99	6.52	5.72	5.38	7.25	5.50	7.82	7.43	11.59
Eu	1.49	1.78	2.99	1.43	1.27	1.50	1.54	1.73	1.42	1.69	1.78	2.27
Gd	5.09	8.38	8.81	5.61	5.92	5.55	5.25	6.92	5.29	7.51	6.74	10.40
Tb	0.69	1.29	1.11	0.82	0.87	0.82	0.76	1.02	0.77	1.08	1.01	1.52
Dy	4.14	7.69	5.40	4.87	5.25	4.84	4.59	6.22	4.65	6.50	6.22	9.15
Ho	0.83	1.62	0.94	1.02	1.12	1.03	0.95	1.31	0.98	1.39	1.26	1.81
Er	2.31	4.52	2.33	2.87	3.26	2.88	2.71	3.75	2.76	3.85	3.45	5.02
Tm	0.33	0.65	0.29	0.41	0.49	0.41	0.39	0.54	0.39	0.55	0.48	0.70
Yb	2.28	4.32	1.69	2.67	3.24	2.67	2.51	3.50	2.53	3.64	3.24	4.56
Lu	0.33	0.66	0.24	0.41	0.51	0.41	0.38	0.54	0.39	0.54	0.46	0.65

table 2A. continued.

Sample	ACH - 157q	CCH-72q	CCH-71q	ACh - 114q	ACH-152q	ACH-150q	ACH - 161q	ACH - 214q	CCH - 83q	CCH - 84q	CCH - 97q	ACH - 171q
Formation	Cerrillos (toba intercalada en lava2)	Cerrillos	Cerrillos	Cerrillos	Cerrillos	Cerrillos	Cerrillos	Cerrillos	Viñita	Viñita	Viñita	Viñita
Age	93	105	100	90	90	90	92	91	81	80	79	84
Lithology	dacite tuff	andesite lava	crystal tuff	welded tuff	welded tuff	welded tuff	andesite lava	andesitic hornfels	andesite lava	basaltic lava	andesite lava	dacite lava
wt.%												
SiO_2	69.27	65.32	53.01	64.73	62.35	65.59	52.72	53.21	55.27	51.73	56.08	70.59
Al_2O_3	14.61	16.34	16.58	14.89	16.34	15.96	17.22	16.80	17.16	17.62	18.83	14.36
TiO_2	0.80	0.26	0.88	0.88	0.89	0.63	1.11	1.27	1.07	0.89	0.86	0.38
Fe_2O_3	4.41	4.23	8.06	5.41	6.01	4.31	10.57	9.45	9.18	9.08	7.42	3.26
CaO	4.72	2.10	7.35	2.32	2.62	1.58	7.93	7.28	8.19	9.02	7.15	1.83
MgO	0.49	0.12	0.39	0.56	1.20	0.70	3.79	2.80	3.40	5.18	3.04	0.94
MnO	0.10	0.05	0.08	0.10	0.07	0.12	0.19	0.26	0.23	0.18	0.12	0.11
Na_2O	2.11	9.17	8.39	4.46	5.15	4.66	4.16	1.55	3.05	2.56	3.56	3.51
K_2O	2.68	0.36	0.09	4.05	4.02	5.31	0.80	6.60	1.04	1.27	0.87	3.94
P_2O_5	0.13	0.11	0.13	0.24	0.13	0.08	0.10	0.20	0.12	0.09	0.12	0.05
LOI	0.21	1.53	4.70	1.93	0.83	0.76	0.91	0.32	0.89	2.01	1.46	0.60
SUMA	99.53	99.58	99.66	99.57	99.62	99.71	99.51	99.74	99.59	99.63	99.51	99.58
ppm												
Cu	42.00	22.00	11.00	20.00	9.00	36.00	46.00	231.00	45.00	65.00	175.00	24.00
Pb	8.00	b.d.l.	12.00	11.00	4.00	16.00	b.d.l.	4.00	8.00	b.d.l.	6.00	11.00
Ni	b.d.l.	b.d.l.	b.d.l.	b.d.l.	b.d.l.	b.d.l.	b.d.l.	12.00	b.d.l.	19.00	b.d.l.	b.d.l.
Co	6.00	b.d.l.	2.00	b.d.l.	6.00	3.00	23.00	23.00	20.00	29.00	19.00	6.00
Zn	56.00	11.00	20.00	66.00	89.00	97.00	75.00	116.00	115.00	94.00	81.00	51.00
Cr	22.63	4.99	31.39	b.d.l.	242.70	10.43	48.91	37.76	39.65	38.49	17.56	20.93
Sc	-	-	-	-	-	-	-	-	-	-	-	-
V	45.50	34.72	26.10	63.16	637.60	719.60	307.90	205.80	285.30	171.30	174.50	42.61
Nb	9.04	7.69	9.35	12.79	9.66	12.01	b.d.l.	6.16	8.65	5.44	0.35	5.15
Zr	333.70	121.20	160.20	384.20	273.90	433.70	65.29	185.90	123.30	74.45	83.70	171.70
U	3.16	1.52	1.67	2.85	7.15	4.95	0.24	0.98	2.09	1.64	0.55	2.83
Th	11.20	5.73	6.00	12.40	26.39	21.43	0.79	3.68	7.00	6.61	1.06	11.97
Rb	90.00	8.00	5.00	138.00	77.00	189.00	34.00	285.00	34.00	30.00	13.00	140.00
Sr	182.30	148.50	760.50	270.20	419.80	232.40	486.50	347.40	344.00	260.20	684.00	173.60
Ba	696.50	34.72	26.10	972.90	637.60	719.60	169.60	527.90	256.60	244.60	373.40	439.90
Y	43.42	18.25	22.36	57.19	39.07	50.30	23.60	29.27	26.70	21.46	15.07	17.51
Cs	1.90	0.26	0.31	2.43	2.40	3.35	2.93	9.56	1.69	1.74	0.35	4.23
Hf	7.99	2.93	2.77	9.23	9.22	11.44	1.37	5.10	4.86	3.16	0.81	3.63
Ta	0.65	0.69	0.47	0.72	0.89	0.97	0.09	0.64	0.72	0.55	0.12	0.35
La	29.39	22.30	19.80	41.76	30.03	38.76	8.68	19.90	14.40	11.93	10.75	20.80
Ce	65.06	46.61	42.05	94.04	70.00	89.66	21.40	47.42	33.18	26.68	24.44	38.37
Pr	8.71	5.47	5.25	11.94	8.94	11.15	2.81	6.20	4.34	3.43	3.17	4.26
Nd	39.36	20.92	21.97	53.93	37.75	46.73	13.82	29.20	20.18	15.85	14.41	16.42
Sm	8.42	3.78	4.74	10.21	8.15	10.00	3.38	6.86	4.60	3.67	3.22	3.03
Eu	1.71	1.04	1.20	1.97	1.66	1.75	1.14	1.67	1.37	1.13	1.03	0.67
Gd	7.54	3.23	4.53	8.94	7.59	9.06	3.64	6.29	4.48	3.64	2.94	2.72
Tb	1.21	0.48	0.67	1.39	1.12	1.38	0.60	0.94	0.74	0.62	0.45	0.42
Dy	7.29	2.92	3.98	8.51	6.71	8.46	3.90	5.80	4.53	3.75	2.71	2.72
Ho	1.59	0.65	0.84	1.84	1.42	1.83	0.84	1.19	0.99	0.82	0.57	0.59
Er	4.52	1.97	2.33	5.25	3.90	5.36	2.39	3.30	2.73	2.30	1.56	1.77
Tm	0.68	0.32	0.33	0.76	0.59	0.82	0.33	0.46	0.42	0.36	0.22	0.27
Yb	4.47	2.24	2.14	5.20	3.82	5.44	2.25	3.06	2.78	2.33	1.45	1.99
Lu	0.68	0.37	0.32	0.81	0.58	0.84	0.32	0.43	0.42	0.35	0.22	0.31

table 2A. continued.

Sample	CCH - 117q	ACH - 191q	ACH - 199q	ACH - 213q	CCH - 116q	CCH - 96q	CCH - 115q	ACH - 203q	ACH - 209q	ACH - 197q	Jo1	Jo2
Formation	Viñita	Viñita	Viñita	Viñita	Viñita	Viñita	Viñita	Viñita	Viñita	Viñita	Johana	Johana
Age	80	76	79	78	80	78	77	78	79	78	87	87
Lithology	dacite lava	basaltic andesite lava	andesite lava	andesitic hornfels	rhyolite dome	welded tuff	rhyolite dome	vitrous tuff	welded tuff	andesite lava	dacite porphyry	dacite porphyry
wt.%												
SiO_2	68.46	53.09	58.54	59.22	72.56	71.60	75.09	70.02	66.36	60.88	68.50	66.20
Al_2O_3	15.98	17.20	18.23	16.76	14.73	14.64	13.53	14.06	15.66	16.66	12.75	16.00
TiO_2	0.39	1.26	0.90	0.84	0.26	0.42	0.09	0.42	0.67	0.83	0.33	0.43
Fe_2O_3	3.32	8.34	6.55	5.96	1.96	3.02	1.27	2.68	3.21	5.25	6.21	5.58
CaO	2.71	6.77	4.06	5.67	2.22	1.33	3.77	2.27	1.60	4.68	2.72	4.16
MgO	1.25	3.44	2.47	3.26	0.40	0.67	0.33	1.11	0.86	2.05	1.25	1.74
MnO	0.14	0.14	0.09	0.10	0.11	0.05	0.07	0.07	0.06	0.09	0.06	0.06
Na_2O	4.57	4.78	3.32	3.86	4.49	2.74	2.69	4.15	4.41	3.70	3.36	4.04
K_2O	2.32	0.47	4.88	3.32	2.02	3.25	1.63	2.11	5.76	3.01	0.77	0.85
P_2O_5	0.08	0.23	0.13	0.11	0.04	0.05	0.03	0.05	0.09	0.12	0.12	0.20
LOI	0.53	4.00	0.64	0.56	0.82	1.87	1.05	2.86	1.04	2.25	2.30	1.29
SUMA	99.76	99.71	99.81	99.67	99.63	99.64	99.56	99.81	99.73	99.52	96.07	99.26
ppm												
Cu	28.00	10.00	45.00	48.00	12.00	7.00	8.00	25.00	15.00	59.00	-	-
Pb	7.00	b.d.l.	6.00	17.00	38.00	9.00	12.00	9.00	11.00	11.00	3.10	2.80
Ni	b.d.l.	2.00	8.00	21.00	b.d.l.	b.d.l.	b.d.l.	6.00	b.d.l.	12.00	-	-
Co	b.d.l.	20.00	15.00	18.00	b.d.l.	5.00	b.d.l.	8.00	3.00	12.00	-	-
Zn	66.00	60.00	72.00	62.00	72.00	47.00	39.00	45.00	51.00	69.00	-	-
Cr	13.56	11.95	15.60	58.06	7.38	12.53	13.84	13.03	10.18	27.76	-	-
Sc	-	-	-	-	-	-	-	-	-	-	-	-
V	14.67	195.10	133.00	138.20	b.d.l.	44.01	b.d.l.	45.30	49.26	107.20	-	-
Nb	6.62	5.69	4.20	7.70	3.95	5.97	11.41	7.00	11.26	6.95	4.00	4.90
Zr	127.70	105.60	121.00	207.10	93.10	253.90	69.05	106.90	309.40	193.60	7.10	18.00
U	1.17	0.79	1.62	2.06	0.73	3.65	3.01	3.00	3.74	2.36	b.d.l.	0.80
Th	4.16	3.50	6.95	8.46	2.62	11.55	8.17	10.26	13.57	8.25	3.00	4.00
Rb	50.00	8.00	176.00	93.00	49.00	131.00	59.00	81.00	176.00	64.00	19.60	18.70
Sr	436.80	635.40	416.10	448.50	241.90	112.70	524.40	130.80	381.60	464.40	334.00	405.00
Ba	604.50	314.00	795.70	623.80	251.80	544.40	477.80	314.30	1066.00	653.20	320.00	490.00
Y	17.72	20.79	13.12	18.17	17.55	30.40	27.92	12.29	20.67	17.12	12.70	16.20
Cs	5.92	0.47	7.82	3.69	2.86	4.39	2.91	2.16	1.58	1.07	3.07	2.79
Hf	3.28	3.37	3.94	5.51	2.51	6.69	2.73	3.52	8.44	5.75	0.30	0.70
Ta	0.78	0.50	0.44	0.81	0.34	0.58	1.24	0.83	1.05	0.66	0.29	0.39
La	20.80	17.19	22.15	23.10	23.15	18.20	20.25	20.20	31.54	22.47	16.40	16.90
Ce	43.30	40.34	47.60	50.20	48.86	41.08	42.26	40.55	68.84	48.29	34.30	33.90
Pr	4.77	4.81	5.18	5.69	5.36	5.39	4.54	4.15	7.43	5.48	4.00	4.30
Nd	19.18	22.64	21.74	24.04	21.51	22.89	17.55	16.05	30.11	22.88	15.10	17.60
Sm	3.73	4.97	4.05	4.76	3.91	4.98	4.15	2.80	5.61	4.50	2.90	3.50
Eu	0.98	1.43	1.20	1.19	1.08	0.80	0.64	0.58	1.17	1.12	0.80	1.00
Gd	3.23	4.61	3.40	4.11	3.23	4.72	4.02	2.36	4.74	3.85	2.30	3.20
Tb	0.50	0.69	0.47	0.59	0.49	0.81	0.72	0.35	0.67	0.57	0.30	0.50
Dy	3.14	4.30	2.77	3.60	3.04	5.14	4.73	2.22	4.11	3.41	2.00	2.80
Ho	0.66	0.85	0.54	0.73	0.65	1.17	1.00	0.47	0.82	0.70	0.40	0.60
Er	1.92	2.31	1.47	2.01	1.89	3.48	2.93	1.35	2.33	1.90	1.30	1.80
Tm	0.29	0.31	0.20	0.28	0.29	0.56	0.43	0.20	0.33	0.27	0.20	0.30
Yb	2.07	2.00	1.33	1.94	2.08	3.85	2.92	1.39	2.29	1.81	1.20	1.90
Lu	0.32	0.27	0.18	0.28	0.32	0.60	0.42	0.20	0.33	0.27	0.20	0.30

table 2A. continued.

Sample	Un1	Un2	PC1	Do1	Do2	Do3	Do4	Do5	Do6	El1	El2
Formation	Mina Union	Mina Union	Pta Colorada	Domeyko	Domeyko	Domeyko	Domeyko	Domeyko	Domeyko	Elisa	Elisa
Age	112	112	110	104	104	104	104	104	104	91	91
Lithology	dacite porphyry	dacite porphyry	dacite porphyry	dacite porphyry	dacite porphyry	dacite porphyry	dacite porphyry	dacite porphyry	dacite porphyry	dacite porphyry	dacite porphyry
wt.%											
SiO_2	63.40	65.20	68.55	60.20	59.90	60.28	67.30	63.92	63.34	73.00	73.70
Al_2O_3	15.60	16.10	15.74	16.20	17.85	18.89	14.60	15.85	17.01	13.30	13.50
TiO_2	0.40	0.40	0.46	0.67	0.59	0.79	0.34	0.71	0.44	0.20	0.24
Fe_2O_3	5.70	5.10	1.56	8.15	6.51	4.79	5.48	5.43	4.99	1.76	2.09
CaO	3.12	3.00	4.11	0.53	1.62	1.20	1.98	2.08	3.64	1.38	1.29
MgO	1.45	1.08	1.75	3.08	2.58	3.57	1.44	2.73	1.95	0.64	0.63
MnO	0.12	0.12	0.06	0.08	0.14	0.07	0.09	0.04	0.04	0.03	0.03
Na_2O	4.65	3.55	5.67	3.90	1.70	6.22	3.97	4.53	3.76	3.01	3.15
K_2O	2.34	2.37	0.54	3.71	3.72	2.44	1.38	2.23	1.32	4.20	4.42
P_2O_5	0.12	0.11	0.14	0.11	0.14	N/D	0.08	N/D	0.01	0.09	0.04
LOI	1.39	2.30	1.14	2.10	3.50	1.68	1.19	2.33	3.38	0.64	0.73
SUMA	96.90	97.03	98.58	96.63	94.75	98.25	96.66	97.52	96.50	97.61	99.09
ppm											
Cu	-	-	-	-	-	-	-	-	-	-	-
Pb	17.90	18.00	b.l.d.	20.30	10.20	-	5.50	-	-	5.70	6.20
Ni	-	-	-	-	-	-	-	-	-	-	-
Co	-	-	-	-	-	-	-	-	-	-	-
Zn	-	-	-	-	-	-	-	-	-	-	-
Cr	-	-	-	-	-	-	-	-	-	-	-
Sc	-	-	-	-	-	-	-	-	-	-	-
V	-	-	-	-	-	-	-	-	-	-	-
Nb	4.00	2.20	5.47	3.30	3.20	3.20	3.60	3.80	3.80	8.00	7.20
Zr	13.50	15.00	93.49	6.60	22.50	89.00	12.30	90.00	75.00	27.70	27.10
U	0.60	0.50	1.23	0.70	1.00	-	1.00	-	-	5.00	6.10
Th	4.00	2.90	4.75	3.00	3.00	1.30	5.00	1.80	3.20	22.00	21.00
Rb	30.60	31.80	20.00	78.60	88.80	-	49.80	-	-	112.00	112.50
Sr	408.00	284.00	442.10	130.50	189.50	216.00	196.50	140.00	370.00	192.00	199.50
Ba	480.00	448.00	112.30	350.00	580.00	290.00	210.00	138.00	250.00	430.00	470.00
Y	18.40	24.40	12.71	12.70	15.60	13.00	22.70	29.00	24.00	13.80	14.40
Cs	0.68	0.90	0.81	5.23	6.22	-	1.99	-	-	3.80	3.52
Hf	0.50	b.d.l.	2.37	0.20	0.50	2.60	0.40	2.60	2.20	1.10	1.00
Ta	0.35	0.30	0.32	0.26	0.28	-	0.32	-	-	0.88	0.76
La	8.20	6.90	19.55	6.20	10.60	8.00	14.40	13.00	17.00	26.30	20.50
Ce	17.80	15.10	39.93	14.00	21.90	15.00	29.80	29.00	34.00	48.70	39.20
Pr	2.60	1.80	4.60	1.80	2.80	-	3.60	-	-	5.50	4.60
Nd	11.60	9.80	18.97	7.60	12.10	7.00	14.50	18.00	15.00	18.40	16.40
Sm	2.60	2.30	2.84	1.80	2.70	1.39	3.30	4.61	3.62	3.10	3.00
Eu	0.80	0.60	0.73	0.60	1.00	0.52	1.20	1.20	1.27	0.60	0.60
Gd	2.80	2.30	2.31	1.60	2.80	1.88	3.20	5.10	3.83	2.40	2.60
Tb	0.40	0.20	0.34	0.30	0.40	-	0.50	-	-	0.40	0.40
Dy	2.60	2.70	1.99	1.80	2.80	2.30	3.20	5.19	4.07	2.10	2.30
Ho	0.60	0.10	0.43	0.40	0.60	0.51	0.70	1.10	0.78	0.40	0.50
Er	2.00	1.60	1.23	1.50	1.80	1.51	2.20	2.89	2.05	1.50	1.60
Tm	0.30	0.30	0.19	0.30	0.30	-	0.30	-	-	0.20	0.30
Yb	1.90	1.70	1.32	1.70	1.80	1.50	2.10	2.93	2.14	1.60	1.70
Lu	0.30	<0.1	0.21	0.30	0.30	0.22	0.40	0.44	0.30	0.30	0.30

Analytical Procedures Table 2A

Rock sample for geochemical analyses were crushed and pulverized under 60 µm. The rock sample was mixed with a 1:3 flux mixture of lithium metaborate and tetraborate. The final proportion of sample and flux mixture is 1:10 and then melt in a glass pearl, alternatively the sample was mixed with binder material (vegetal wax and boric acid) and pressed in a briquette, for major or trace elements (Cu, Pb, Ni, Co, Zn, Cr, Sc, V, Zr, Rb, Sr, Ba) , respectively. The concentration of major elements represented as oxides in weight percent (wt%) has been measured by X-ray Fluorescence in the chemical Laboratory of SERNAGEOMIN using a Panalytical AXIOS equipment. The concentration of a set of trace elements indicated above was measured in the same equipment, and expressed in parts per million (ppm). Another part of the crushed sample was dissolved by fussion using a 4:1 mixture of Na_2CO_3:$L_2B_4O_7$ and acid attack with HNO_3 and used to measure the concentration in ppm of rare Earth Elements (REE: La, Ce, Pr, Nd, Sm, Eu, Gd, Tb, Dy, Nb, Ho, Er, Tm, Yb, Lu) and some trace elements (U, Th, Y, Cs, Hf, Ta) by ICP-MS (Inductive Coupled Plasma Mass Spectromety) using an Agilent 7500 equipment.